Alloy element redistribution during sintering of powder metallurgy steels

by

Abdul Malik Tahir

Doctoral Thesis in Engineering Mechanics

May 2014
Technical Reports from
Royal Institute of Technology
Department of Mechanics
SE-100 44 Stockholm, Sweden

Akademisk avhandling som med tillstånd av Kungliga Tekniska Högskolan i Stockholm framlägges till offentlig granskning för avläggande av teknologie doktorsexamen måndag den 26 May 2014 kl 10.15 i sal F3, Kungliga Tekniska Högskolan, Lindstedsvägen 26, Stockholm.

Universitetsservice US–AB, Stockholm 2014

Proclaim! (or read!) in the name of thy Lord and Cherisher, Who created- Created man, out of a (mere) clot of congealed blood: Proclaim! And thy Lord is Most Bountiful,- Who taught (the use of) the pen,- Taught man that which he knew not.

Quran, sura 96 (Al-Alaq), ayat 1-5.

To my brother, Abdul-Khaliq

Alloy element redistribution during sintering of powder metallurgy steels

Abdul Malik Tahir
KTH Mechanics
SE-100 44 Stockholm, Sweden

Abstract

Homogenization of alloying elements is desired during sintering of powder metallurgy components. The redistribution processes such as penetration of liquid phase into the interparticle/grain boundaries of solid particles and subsequent solid-state diffusion of alloy element(s) in the base powder, are important for the effective homogenization of alloy element(s) during liquid phase sintering of the mixed powders. The aim of this study is to increase the understanding of alloy element redistribution processes and their effect on the dimensional properties of the compact by means of numerical and experimental techniques.

The phase field model coupled with Navier-Stokes equations is used for the simulations of dynamic wetting of millimeter- and micrometer-sized metal drops and liquid phase penetration into interparticle boundaries. The simulations of solid particle rearrangement under the action of capillary forces exerted by the liquid phase are carried out by using the equilibrium equation for a linear elastic material. Thermodynamic and kinetic calculations are performed to predict the phase diagram and the diffusion distances respectively. The test materials used for the experimental studies are three different powder mixes; Fe-2%Cu, Fe-2%Cu-0.5%C, and Fe-2%(Cu-2%Ni-1.5%Si)-0.5%C. Light optical microscopy, energy dispersive X-ray spectroscopy and dilatometry are used to study the microstructure, kinetics of the liquid phase penetration, solid-state diffusion of the Cu, and the dimensional changes during sintering.

The wetting simulations are verified by matching the spreading experiments of millimeter-sized metal drops and it is observed that wetting kinetics is much faster for a micrometer-sized drop compared to the millimeter-sized drop. The simulations predicted the liquid phase penetration kinetics and the motion of solid particles during the primary rearrangement stage of liquid phase sintering in agreement with the analytical model. Microscopy revealed that the C addition delayed the penetration of the Cu rich liquid phase into interparticle/grain boundaries of Fe particles, especially into the grain boundaries of large Fe particles, and consequently the Cu diffusion in Fe is also delayed. We propose that the relatively lower magnitude of the sudden volumetric expansion in the master alloy system could be due to the continuous melting of liquid forming master alloy particles.

Descriptors: Contact line friction, Cu redistribution kinetics, diffusion, dimensional variations, dilatometry, DICTRA, dynamic wetting, liquid phase sintering, master alloy, microstructure, phase field modeling, primary rearrangement, powder metallurgy steels, SEM/EDXS, swelling, Thermo-Calc.

Omfördelning av legeringselement under sintring av pulvermetallurgiska stål

Abdul Malik Tahir
KTH Mekanik
SE-100 44 Stockholm, Sverige

Sammanfattning

Homogenisering av legeringselement är önskvärd under sintring av pulvermetallurgiska komponenter. Omfördelningsprocesser såsom penetrering av vätskefasen in i partikel- eller korngränserna och efterföljande solid-state diffusion av legeringselement i baspulvret, är viktiga för effektiv homogenisering av legeringselement under vätskefassintring av pulver blandningar. Syftet med denna studie var att med hjälp av numeriska och experimentella tekniker öka förståelsen om omfördelningsprocesser vid sintring och deras inverkan på dimensionsförändringar hos de sintrade detaljerna.

Fasfältsmodellen i kombination med Navier-Stokes ekvationer användes för simulering av dynamisk vätning av millimeter- och mikrometerstora metalldroppar och vätskepenetration i partikelgränser. Simuleringarna av partikelomfördelning under inverkan av kapillära krafter som utövas av den flytande fasen genomfördes genom koppling av jämviktsekvationen för ett linjärt elastiskt material och Cahn-Hilliards och Navier-Stokes ekvationer. Termodynamiska och kinetiska beräkningar utfördes för att förutsäga diffusionsavstånd och materialsystemets fas diagram. De testmaterial som användes för de experimentella studierna var tre olika pulverblandningar; Fe-2%Cu, Fe-2%Cu-0.5%C, och Fe-2%(Cu-2%Ni-1,5%Si)-0.5%C. Optisk mikroskopi, energi dispersiv röntgenspektroskopi och dilatometri användes för att studera mikrostruktur, kinetik i vätskepenetrationsfasen, diffusion av Cu i fast fas, och dimensionsförändringar under sintring.

Vätningssimuleringarna verifierades genom att noggrant matcha simuleringar med spridningsexperiment med millimeterstora metalldroppar. Det visar sig att vätningskinetiken är mycket snabbare för en mikrometerstor droppe jämfört med den millimeterstora droppen. Simuleringarna förutspådde vätskefasens penetration och de fasta partiklarnas rörelse under det primära skedet av vätskefassintringen i enlighet med den analytiska modellen. Mikroskopi avslöjar att tillsats av kol fördröjde penetrationen av Cu rik vätskefas in i partikel och korngränser, i synnerhet i korngränserna i stora Fe partiklar, och följaktligen Cu diffusion i Fe. Det föreslås att den möjliga orsaken till den relativt sett lägre plötsliga expansionen av masterlegeringssystemet skulle kunna vara den kontinuerliga smältningen av masterlegeringspartiklar, jämfört med partiklar av ren koppar.

Deskriptorer: Kontaktlinjefriktion, Cu omfördelningskinetik, diffusion, dimensionsvariationer, dilatometri, DICTRA, dynamisk vätning, smältfas sintring, mikrostruktur, fasfältsmodellering, pulvermetallurgiskt stål, SEM/EDXS, Thermo-Calc.

Preface

In the first part, an overview of the PM manufacturing process, basic theory of the related problems, methods employed for the investigations, and brief summary of the results are presented. The second part consists of the following papers;

Paper 1. Tahir, A. M., Amberg, G. and Do-Quang, M.: Initial rapid wetting in metallic systems. *Acta Materialia*, 2013 **61**, 5375.

Paper 2. Tahir, A. M., Amberg, G., Hedström, P., Bergman, O. and Frisk, K.: Investigation of Cu distribution and porosity in Fe-2Cu and Fe-2Cu-0.5C compacts. *Proc. EuroPM2013, Göteborg, Sweden*, 2013, EPMA, **2**.

Paper 3. Tahir, A. M., Amberg, G., Hedström, P., Bergman, O. and Frisk, K.: Cu redistribution during sintering of Fe-2Cu and Fe-2Cu-0.5C compacts. *Powder Metallurgy*, in press, doi.org/10.1179/1743290114Y.0000000085.

Paper 4. Tahir, A. M., Amberg, G., Hedström, P., Bergman, O., Chasoglou, D. and Frisk, K.: Behavior of master alloy during sintering of PM steels; redistribution and dimensional variations. *submitted to Powder Metallurgy.*

Paper 5. Tahir, A. M., Amberg, G. and Malik, A.: Modeling of the primary rearrangement stage of liquid phase sintering. *To be submitted.*

The author has presented part of this work in the following presentations;

Alloy element redistribution in PM steels, *HERO-M Workshop, Sweden* 2009, 2010 and 2013.

Phase field modeling of the alloy element(s) distribution during sintering, *Höganäs chair 2009, Sweden*.

Modeling the initial rapid wetting of Cu during sintering, *EUROMAT 2013, Spain*.

Investigation of Cu distribution and porosity in Fe-2Cu and Fe-2Cu-0.5C compacts, *EuroPM2013, Sweden*.

Division of work between authors;

Paper 1
The code was implemented by Minh Do-Quang (MDQ) and Abdul Malik Tahir (AMT). AMT performed the simulations with feedback from Gustav Amberg (GA). AMT analyzed the results and wrote the paper, with feedback from GA and MDQ.

Paper 2
AMT analyzed the results and wrote the paper, with input from Peter Hedström (PH), GA, Ola Bergman (OB), and Karin Frisk (KF). Sintering trials were performed by Swerea KIMAB AB. The microstructure analysis was done by the Metallography department, Höganäs AB and AMT.

Paper 3
OB and KF planned the experimental work together with AMT. Sintering trials were performed by Swerea KIMAB AB. The microstructure analysis was done by AMT at the Metallography department, Höganäs AB with the help of Heike Grosser. The diffusion measurements were performed at the Dept. of Materials Science and Engineering KTH by AMT and PH. AMT analyzed the results and wrote the paper, with input from PH, GA, OB, and KF.

Paper 4
AMT and OB designed the experimental work. Sintering trials were performed by Swerea KIMAB AB with feedback from AMT. The microstructure analysis was done by AMT at the Metallography department, Höganäs AB together with Heike Grosser. The diffusion measurements were performed at the Dept. of Materials Science and Engineering KTH by AMT with feedback from PH. AMT analyzed the results and wrote the paper, with input from PH, GA, OB, KF, and Dimitris Chasoglou (DC).

Paper 5
Amer Malik (AM) set the numerical model and performed simulations together with AMT. AMT analyzed the results and wrote the paper, with feedback from AM, GA, and OB.

Contents

Part I

Summary

CHAPTER 1

Introduction

The process of manufacturing metallic components from metal powder is called powder metallurgy (PM). The earliest uses of PM technology can be traced back several thousand years. For instance, ancient Incas converted platinum grains into consolidated form and Egyptians hammered metallic iron powder to produce tools (German (1994)). Modern development of PM technology is attributed to the production of cemented carbides in the 1900-1930s (Schwartzkopf *et al.* (1960), which led to a revolution in the tool industry. The large-scale production of structural steel parts by PM method started after World War II. The low cost benefit of PM technology compared to the traditional manufacturing processes continuously boosted the production of PM structural steel parts and today their share in the PM products is among the highest.

The main advantages of PM compared to other conventional metal forming techniques are; near net-shape components, high production rate, low consumption of energy, tailored microstructures, and high material utilization (German (1994)). The near net-shape feature of the PM technology reduces the production cost as fewer or no secondary operations are required. The production of high melting point refractory metals at lower cost and with less difficulty is another advantage of PM. Moreover, the high material utilization and energy efficiency makes the PM production process environmental friendly (MPIF (2014)). The PM components used in the automotive industry i.e., bearings, valve seats, engine timing components etc, reflects a good example of economically produced parts with precision. And the production of materials such as porous filters, oxide-dispersion-strengthened turbine alloys, cermets and artificial bones illustrate the capacity of PM method to produce materials with unique properties and microstructure (German (2005)).

The PM process mainly consists of mixing powdered materials (blending), pressing to obtain the desired shape (compaction) and heating the compact to bond the powder (sintering). Optional post processing operations i.e., machining, grinding, sizing, heat treatment etc, could be further employed. During sintering of the powdered compacts the important criteria for the proper distribution of the liquid phase throughout the solid matrix are: 1, melting of the liquid forming additives (elemental or master alloy) below normal sintering temperatures; 2, good wettability of the molten phase; 3, removal of oxides; 4, the dissolution effects. Although it is desired that the liquid phase should wet and spread over the solid particles and act as a vehicle to improve the homogenization of the alloying elements, in order to tailor desired properties of the final product. At the same time dimensional instabilities caused by the liquid penetration could be detrimental for the final tolerances of the finished

product. Moreover, the rapid kinetics of the melt formation, subsequent liquid penetration and associated changes of the microstructure make it difficult to understand and tailor these processes.

1.1. Motivation and scope of the work

The quantitative treatment of the overall process of liquid phase sintering (LPS) is hindered because of the complexities involved such as various solubility, viscosity, and diffusivity effects coupled with the multiple phases. The rapid nature of the events during rearrangement stage of LPS also poses a challenge for experimental investigations. The main objective of this work is to quantitatively investigate the processes responsible for the homogenization of alloying elements such as wetting, liquid phase distribution, solid-state diffusion, and the associated dimensional changes. Moreover, the numerical models were implemented to predict the kinetics of micro scale events of rapid nature, which could be very challenging to investigate experimentally.

In this work, numerical tools were applied to study the rapid dynamic wetting, penetration of the liquid phase, and particle motion during the primary rearrangement stage of LPS using realistic physical material properties. Thermodynamic and kinetic calculations were employed using DICTRA and Thermo-Calc. In addition, interrupted sintering trials of the test materials were performed in N_2/H_2 (90/10) atmosphere for different holding times at 1120^oC, to investigate the kinetics of redistribution processes during sintering. The microstructure evolution, and the kinetics and extent of the liquid phase penetration were analyzed by light optical microscopy. Dilatometry was used to investigate the dimensional change of the compact during sintering. Energy dispersive X-ray spectroscopy was applied to study the kinetics of the solid-state diffusion of Cu at the Fe interparticle boundaries.

CHAPTER 2

Processing route for powder metallurgy steels

The PM process consists of three main steps i.e., blending, compaction and sintering. Powder fabrication and the alloying of the base powder is done prior to the blending step. Optional secondary operations can be performed after sintering step to enhance the properties of the product. The production route is shown schematically in Fig. 2.1.

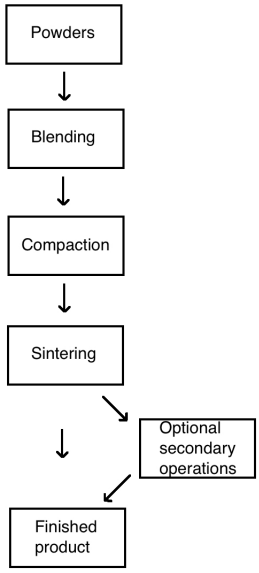

Figure 2.1: Schematic illustration of powder metallurgy production process (author's illustration).

2.1. Powder fabrication

The main techniques for the powder fabrication are mechanical and chemical, as well as electrolytic and atomization (German (2005)). In all these powder producing methods, energy is supplied to create surface free area. The choice of the production technique mainly depends upon the cost, required characteristic of the powder and the intended application. The Fe and steel powder is mostly produced by the chemical fabrication (Höganäs sponge iron process) and water atomization technique. Here,

the emphasis will be only given to the water atomization technique, since the water atomized Fe powder is used in the present work.

Water is commonly used for low reactive materials, with the melting point approximately below 1600^oC (German (2005)). In the water atomization process, the impact of high pressure water jets forces the disintegration of the melt stream. The disintegrated particles are rapidly quenched and therefore particles produced by this method are usually irregular and rough as shown in Fig. 2.2.

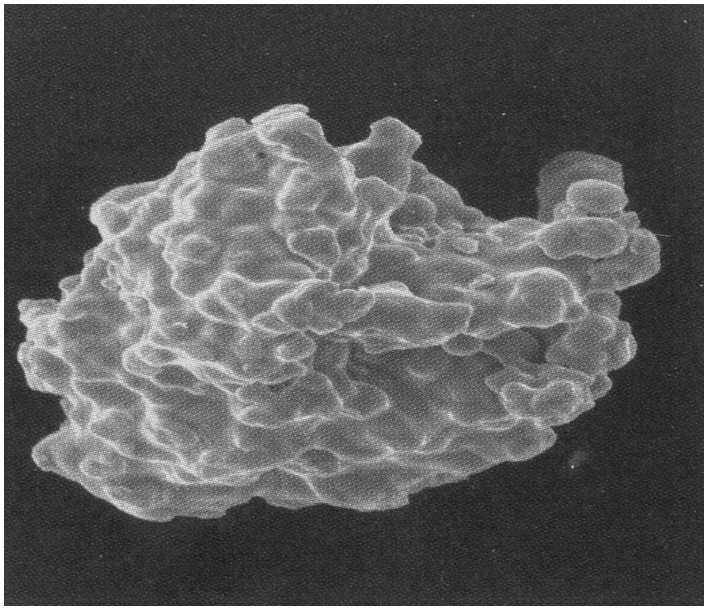

Figure 2.2: Water atomized Fe powder ($\sim$75 μm), ASC100.29 (re-printed from (Höganäs Handbook - 6)).

The size of the particles is mainly controlled by the water jet pressure; higher jet pressure results in higher velocity and which produces smaller particle size. The effect of distance between the nozzle and the water jet stream is not so significant in case of water atomization as compared to air atomization. The possible contaminations during the atomization process might be removed by heating the powder in hydrogen or vacuum, and subsequent milling can be performed to breakup any possible bond formation during heating. A sketch of the typical water atomization process is given in Fig. 2.3.

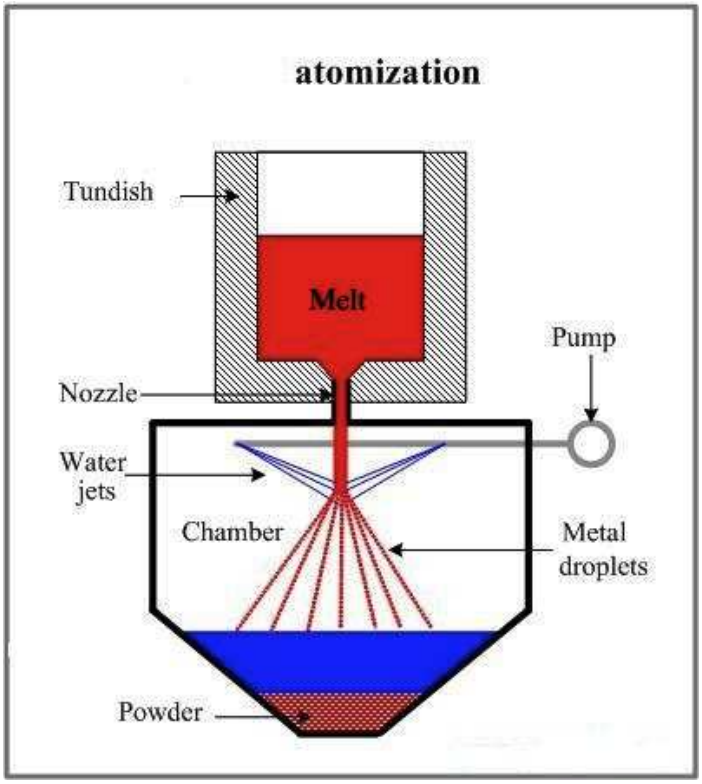

Figure 2.3: Schematic illustration of the water atomization process (re-printed from (substech.com 2014))

2.2. Powder alloying

The purpose of adding alloying elements is mainly to increase the hardenability and strength of sintered components. The common alloying elements in PM steels are carbon (C), copper (Cu), phosphorous (P), nickel (Ni) and molybdenum (Mo). Commercial sintered products produced today are usually based on the above mentioned elements and their alloy systems (Petzow *et al.*, (1980)) such as Fe-Cu, Fe-Cu-C, Fe-Cu-Ni, Fe-Cu-Ni-C etc. Cu is an austenite stabilizer and shows good wettability of the Fe powder and thus spreads rapidly into the pore network of the solid skeleton. Usually the Cu content in sintered steels ranges between 2 and 10% (mass). At normal sintering temperatures (1120^{o}C), approximately 8% of Cu is dissolved by the austenite phase. Swelling of the Cu-alloyed sintered steels is a well known phenomena, which is caused by the penetration of the molten Cu into the Fe interparticle/grain boundaries. C is the most effective alloying element to achieve desired mechanical properties of the sintered steels. Moreover, C addition also compensates the expansion caused by the Cu penetration into Fe interparticle boundaries. Ni is another important alloying element used in PM steels. It is an austenite stabilizer but the diffusion of Ni in austenite is very slow and homogenization can take long time. The slow redistribution of Ni during sintering can produce Ni-rich regions, and provided

that the Ni content is sufficiently high, the austenite structure may be found in the sintered microstructure after cooling. Mo increases hardenability more than Cu and Ni, and also improves the material strength at higher temperatures.

The proper method for adding alloying elements is very important and if not done adequately, may cause the uneven distribution and segregation of the alloying elements in the powder compact. Basically there are three methods for the addition of elemental powders in sintered steels i.e., mixing, partial pre-alloying and fully pre-alloyed. In mixing, the elemental powders are mixed before the compaction and subsequent heating will bond the particles together. This method may cause inhomogeneous distribution of the alloying elements, and also segregation of the powder mixes. In case of partially pre-alloyed powders, segregation of the particles is avoided and homogenization level is enhanced. This is done either by annealing, where bonds will form between powder particles, or with the aid of some organic binder. Mixing the alloying elements in the melt before powder fabrication produces the fully pre-alloyed powders and the maximum level of homogenization is achieved after sintering.

Mixed powders are the best in terms of compressibility and show relatively higher green density at a given pressure. While the partially pre-alloyed powders have almost the same level of compressibility and the fully pre-alloyed powders show the lowest green density. The choice of the alloying method also depends upon the oxidation sensitivity and diffusion rate of the alloying elements. For instance, C diffusion is much faster than Cu or Ni, so it is admixed in the Fe powder, while the Mn and Si are preferentially introduced by the pre-alloying method to avoid oxidation.

2.3. Blending

In sintered steels, the Fe powder is mixed with alloying elements and some organic compounds. The objective of the blending step is to produce a homogenous powder mix. The proper mixing of lubricant is also required to reduce the friction between die walls and powder particles. In addition, the lubricant also improves the sliding of the powder during compaction and results in uniform density from top to bottom. Common lubricants are stearic acid, metallic stearates (zinc stearate) and waxes. Moreover, less friction between die walls and powder makes it easier to eject the compact and minimizes the risk of crack formation in the green compact. The lubricant should be burn off during pre-heating or in the start of sintering process otherwise the residue might affect the compact strength.

2.4. Compaction

Compaction is performed to convert loose powder into a shaped object with enough strength for further processing. The powder particles under pressure densifies, first by sliding past one another and then by deformation as shown in Fig. 2.4. The apparent density of the powder is low before compaction and no bonding exist between the particles. As pressure is applied, the powder particles rearrange, deform and bond together. Relatively more pressure is required to further increase the density after the deformation hardening of particles. The compaction pressure ranges approximately between 100 - 1000 MPa, mainly depending upon the type of powder. In ferrous PM, the common compaction pressure used is approximately 600 MPa.

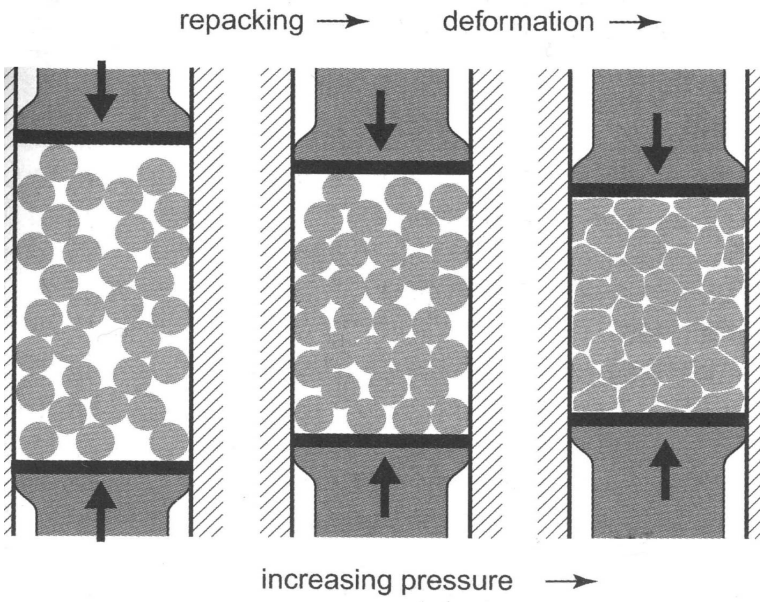

Figure 2.4: Illustrative sketch of the compaction stages (re-printed from (German 2005)).

The process of die compaction and simplified shapes of die and punches are shown in Fig. 2.5. The compaction pressure is applied uniaxially and the die provides the lateral support to the powder. The powder is poured into the die cavity with the help of a feed shoe. During filling the upper punch is retracted and the lower punch is fixed, as it determines the amount of powder for filling. The powder flow should be controlled to avoid undesired density variations in the pressed compact. However, the lower punch might be moved to achieve uniform powder distribution in the die cavity. The powder is usually moved, with the help of the lower punch, near the center of the die after filling to start compaction. After pressing, the upper punch is lifted and the pressed compact is ejected by moving the lower punch. The force required to eject the pressed compact is termed ejection force; the lubricant play a significant role to decrease the ejection force and also the die wear. The die compaction is generally classified into, single-action pressing and double-action pressing. In single-action pressing, the bottom punch is held stationary and the upper punch moves to press the powder. Whereas, the pressure is applied both by the lower and upper punches in the double-action pressing. The density variation in the pressed compact is less uniform in single-action pressing compared to the double-action pressing. The pressed compact is called green compact, and the strength is termed green strength.

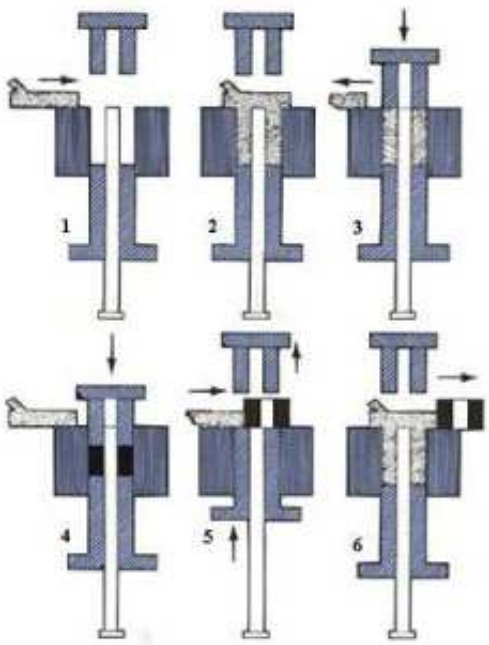

Figure 2.5: Schematic illustration of the die compaction stages (re-printed from (MPIF 1999).

Cold-compaction is the most common method in the mass production of sintered steels, and there are many options in die compaction methodology to achieve higher densities; heating the powder and/or die, soft and hard tooling, changing the dwell time of pressure. In warm-compaction the powder and tool is heated up to approximately 150^{o}C prior to compaction. Cold isostatic pressing (CIP) is another method to increase the density of the green compact and generally used to produce complex shapes. Here, the powder is sealed into flexible tool and pressurized in a vessel filled with a fluid i.e., oil or water. High Velocity Compaction (HVC) is also used for the compaction of sintered steels. This method involves compaction in less than 20 ms by a high energy impact and further densification is achieved by multiple impacts.

2.5. Sintering

Sintering can be defined as a heat treatment process to densify the powder compact. The densification is achieved by bond formation between powder particles, below the melting temperatures via solid-state diffusion process or might involve the formation of liquid phase. The bond between the touching particles results in neck formation (Fig. 2.6), which increases the strength of the compact. Sintering is basically governed by the reduction of the surface energy of particles and the motion of atoms at high temperatures. The particle free surface energy per unit volume is inversely proportional to the particle size, thus the driving force for sintering is higher for the smaller particles and so the sintering rate is faster. Fundamentally sintering can be

explained in these terms; the surface energies associated with the surface curvature provides the *driving force* for the mass transfer, and the method of the atomic motion (mass transfer) defines the *mechanism* of sintering, and the resulting changes in the geometrical features (neck development, grain growth etc) of the particles show the sintering *stages*.

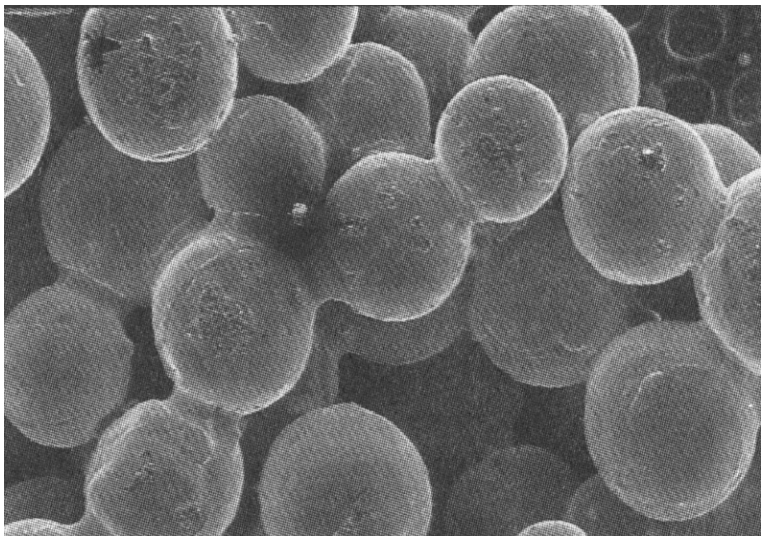

Figure 2.6: Neck formation in the bronze spherical powders (re-printed from (German 2005)).

The atomic mobility is strongly affected by the temperature and the increase in temperature will also increase the number of atoms who can break their bonds and jump to a new site. At high temperature, the atoms will move around randomly and some of them might land at the contact point (bond) between the particles where the bond formation reduces the surface area and thus reduces surface energy. So, the growth of the bond between the particles depends upon the number of atoms landing at the contact point. And the role of heating during sintering is to increase the number of the total atomic jumps, since only some of them will land at low energy zone (bond). Over the time, the enormous number of successful atomic jumps at high temperature significantly changes the microstructure and sintering progresses. One important parameter to monitor during the sintering process is neck growth evolution. The neck-size ratio is defined as X/D, where X is the neck diameter and D is the particle diameter as shown in Fig. 2.7. The longer sintering times and/or increase in temperature favor the neck growth and the neck-size ratio increases.

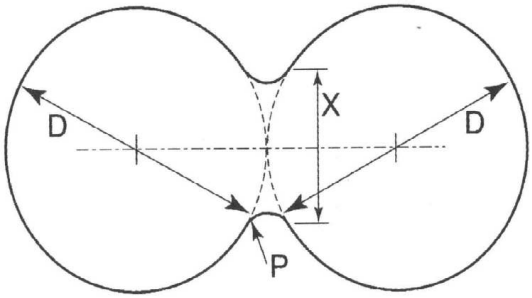

Figure 2.7: Schematic profile of the neck formation between two particles during sintering (re-printed from (German 1985)).

The bulk properties of the compact i.e., density, dimensions etc, undergo changes during sintering and can be used to follow the sintering process. Dimensional changes during sintering are of great importance as they are related to the density change of the compact. Shrinkage, dL/L_o(swelling might also occur) densifies the green compact from green density (ρ_g) to the sintered density (ρ_s) and the relationship between linear shrinkage and the density change is given by Eq. 2.1. Another important measure is the densification, Ψ, defined as the ratio between the change in density due to sintering to the density change required for achieving theoretical density, ρ_t (Eq. 2.2).

$$\rho_s = \rho_g/(1 - dL/L_o)^3 \tag{2.1}$$

$$\Psi = \frac{\rho_s - \rho_g}{\rho_t - \rho_g} \tag{2.2}$$

2.6. Liquid phase sintering

Liquid phase sintering (LPS) and solid state sintering (SSS) are the two major classifications of pressure-less sintering technique (German (1985)). The understanding of the SSS of single component materials is relatively better than the LPS technique, despite of its large-scale industrial applications. Important technical advances in LPS started in the 1930s with development of materials such as cemented carbides (WC-Co), copper alloyed steels (Fe-Cu-C) and cermets. The theoretical basis for the understanding of the LPS is provided by Price *et al.* (1938). Many qualitative models of LPS were developed based on the observations from a variety of systems (Lenel (1948), Huppmann *et al.* (1976), Kingrey (1959), Froschauer *et al.* (1975)). Eremenko *et al.* published a brief treatment of LPS in 1968 and it was followed by a more detailed work in (Eremenko *et al.* (1970)).

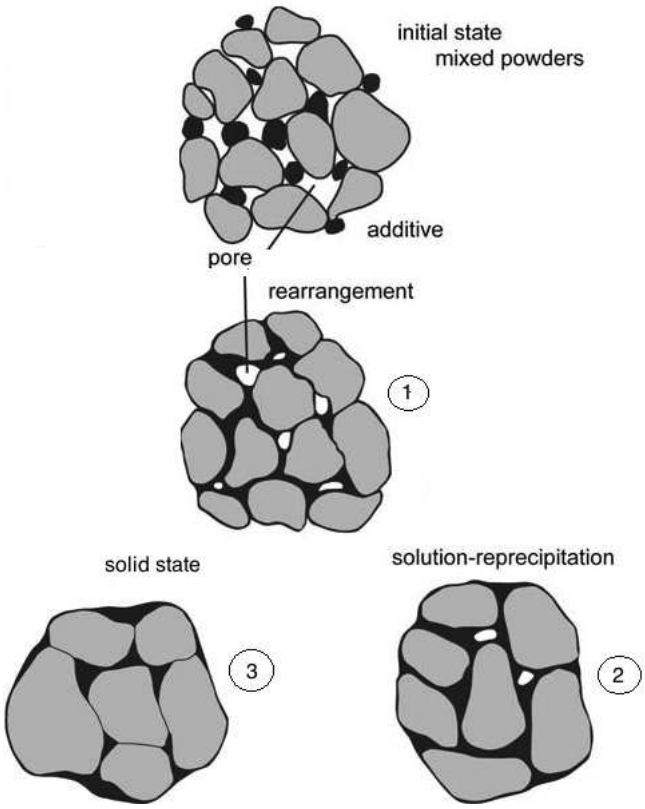

Figure 2.8: Stages of the classic liquid phase sintering process involving mixed powders (re-printed from (German 1985)).

The classic description of LPS is attributed to the work on tungsten heavy alloys (Price *et al.* (1938)). In this case, liquid phase co-exist with the solid particles (persistent) throughout the high temperature part of the sintering cycle. The LPS process can be categorized into three overlapping stages (Moon (1971), Bauer *et al.* (1975), Huppmann *et al.* (1976), Huppmann *et al.* (1979), Yoon *et al.* (1979), Tendolkar *et al.* (1979), German *et al.* (1982)). The schematic sequence of these overlapping stages is shown in Fig. 2.8. The stages are named as: 1. Rearrangement, 2. Solution-reprecipitation, 3. Solid state. The microstructural changes associated with the above mentioned stages are shown in Fig. 2.9.

The rearrangement stage of the LPS involves melt distribution into pores between the solid particles and rapid densification occurs because of capillary forces exerted by the wetting liquid on the solid particles. The compact acts as a viscous body, where solid particles can slide/rearrange themselves to improve densification. The elimination of the porosity is achieved by the reduction in the surface energy and increase in the compact viscosity. Thus, the resistance to rearrangement increases and the densification rate progressively slows down. The main events in this stage are, repacking, rapid densification or swelling and particle sliding. The amount of

densification during this stage depends upon the particle size, volume fraction of liquid and the solubility of solid in the liquid. The rearrangement process is usually more effective in case of finer particles. The full density is only achieved, when enough amount of liquid is formed. It is estimated that for achieving full density in the rearrangement process, approximately 35% (volume) of the liquid phase is required. High green densities and the irregular shapes of the particle might inhibit the densification during the rearrangement process.

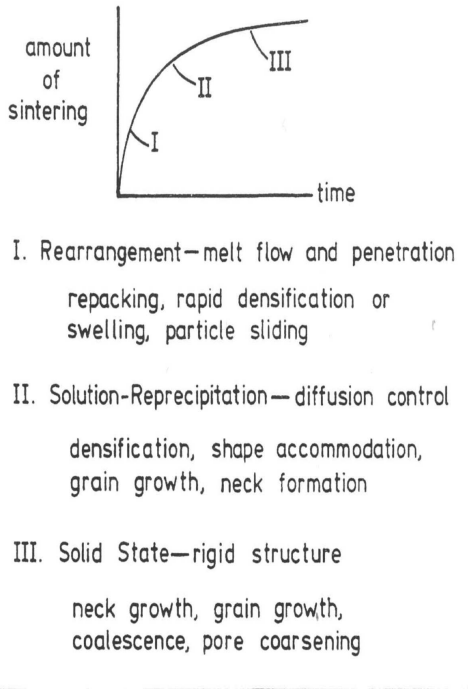

Figure 2.9: The events associated with different stages of the liquid phase sintering (re-printed from (German 1985)).

The next stage of LPS is termed solution-reprecipitation. The general characteristic of this stage is the microstructural coarsening. This is mainly caused by the particle size distribution in the compact. The solubility of the solid grain into the liquid is inversely proportional to the grain size; smaller particle will dissolve more into liquid phase compared to larger particles. This will cause a concentration gradient in the liquid and then the material will be transported from higher concentration regions to the lower concentration areas. Thus, the materials will be transferred from the smaller particles to the larger particles and eventually, the bigger particles will grow. This phenomena is known as Ostwald ripening or coarsening. The particle shape accommodation is another important process active during this stage. This allows the tighter packing of the solid particles and enhances densification. Both coarsening and particle shape accommodation are affected by the amount of liquid.

The geometrical shape of the solid particles is determined by the solid-solid and solid-liquid interfacial energies, amount of liquid, and the anisotropy in the surface energy of the solid particles. The final stage of LPS is the solid state controlled sintering. Here, the densification is slow because of the formation of solid skeleton. The remaining pores might grow, if they contain any entrapped gas, to reduce the pressure.

The processes dominant in the different stages are actually active throughout the sintering cycle, but their significance to the change in bulk properties such as density depend upon the sintering stage. For instance, the kinetics of the rearrangement stage (melt penetration) is so fast that the diffusion effects are negligible. The densification rate during this stage is also very high and decreases as the solution-reprecipitation stage becomes significant. A general trend for the increase in densification during different stages of LPS is shown in Fig. 2.10.

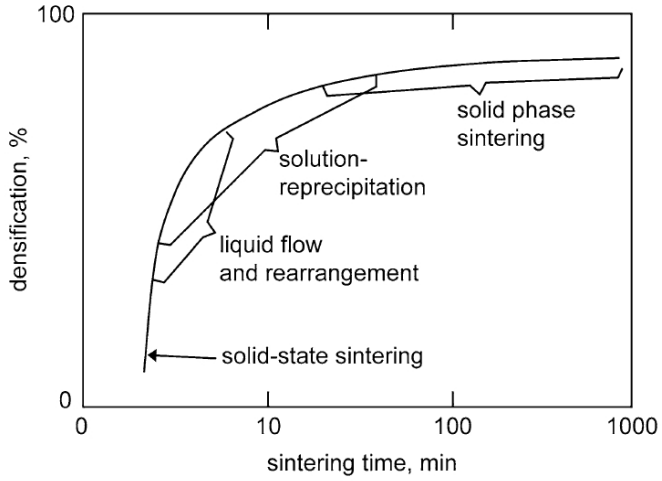

Figure 2.10: General densification trend during the overlapping stages of the liquid phase sintering.

CHAPTER 3

Alloy element redistribution and dimensional variations

Alloying of the Fe powder is very common for optimizing the desired properties of the final product. In case of elemental or partially pre-alloyed powder mixes, it is usually desired that the proper homogenization of the alloying elements is achieved. The presence of liquid phase (persistent or transient) acts as a vehicle for the alloying elements, which rapidly redistribute them into the solid matrix. This will coat the solid particles by a liquid layer (depending upon the amount of liquid) and increases the effective cross-section for the solid-state diffusion of the alloying elements. As sintering is basically the diffusion (motion) of atoms that is why the liquid phase enhances the sintering mechanism. Hence, in general liquid phase not only enhances the sintering mechanism but also provides a faster channel for the redistribution of alloying element.

As always there are some disadvantages, the dimensional variation associated with the rapid distribution of the liquid phase is one such effect of the LPS. The faster kinetics of the liquid phase penetration makes it more difficult to control the dimensional variations and they might affect the final dimensional tolerances of the product. According to the heavy alloy mechanism (Lenel (1948)) the significant rearrangement of the solid particles for the densification of the compact on melt formation is dependent on five criteria; solubility of solid in the liquid, low contact angle, small dihedral angle, low degree of solid state interparticle bonding, and loose powder structure. The probability of swelling increases as fewer of these criteria are fulfilled. The first three criteria mentioned above are the material parameters, while the last two are the processing conditions. There are several other processing factors like green density, heating rate and particle size, which can also effect the rearrangement of solid particles. So the basic criteria might not show the complete picture, but still they are a good starting point for predicting the overall behavior of a system.

Here, the focus is on the events occurring shortly after melt formation i.e., melt penetration, particle rearrangement and the consequent dimensional changes. These initial factors could also effect the solid-state diffusion of the alloying elements at the solid interparticle boundaries. In LPS, wetting capacity of a liquid phase for a given solid surface is one of the most significant parameter. Good wettability of the liquid phase will effectively redistribute the melt into the interparticle boundaries, and homogenization level could be greatly enhanced. The wetting liquid spread under the action of the capillarity and reactivity. After melt formation the liquid phase penetrates into the channels between solid particles and subsequently into the grain boundaries of the polycrystalline solid particles as shown in Fig. 3.1. The kinetics of the pore penetration is very fast and an estimate of the rate of penetration (Eq. 3.1) is given by Pejovnik *et al.* (1979). σ is the surface energy, r is the pore radius and μ is the viscosity. However, mutual solubility between the base and additive (liquid former)

also affects the spreading/penetration kinetics. The dissolution processes between the solid and liquid phase improves the wetting but the kinetics of the spreading becomes slow. In addition, the melting behavior (precise melting point or melting over a range) of the additive phase is also important in determining the distribution of the liquid phase and how it effects the dimensional variations. Moreover, the presence of oxides on the solid particles inhibits the proper wetting of liquid phase.

$$x^2 = \sigma \cdot r \cdot t \cdot cos\theta / 2\mu \tag{3.1}$$

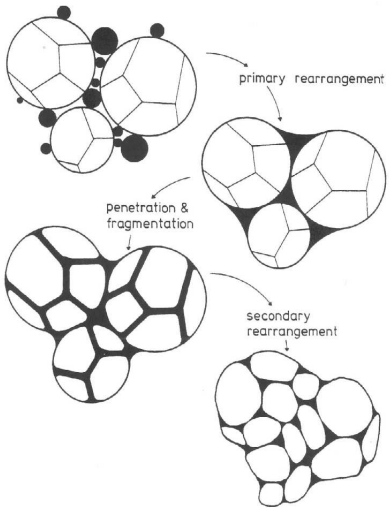

Figure 3.1: Schematic illustration of the melt penetration into interparticle and grain boundaries and the consequent rearrangement (re-printed from (German 1985)).

In general melt formation (spreading/penetration) and the mutual solubility among the components of the system are the important material parameters in determining the dimensional behavior of the compact during rearrangement stage; shrinkage or expansion. A high solid solubility in the liquid helps densification by rearrangement, whereas high solubility of the liquid in the solid coupled with the low solubility of the solid in the liquid gives swelling. The solubility ratio S_R is defined as, $= S_B/S_A$. S represent the solubility, where the subscript B is the base (major phase) solubility in the additive and A is the additive solubility in the base. The schematic of the shrinkage and expansion is shown in Fig. 3.2. The densification because of high solid solubility in liquid is related to the lubrication and surface smoothing of solid particles.

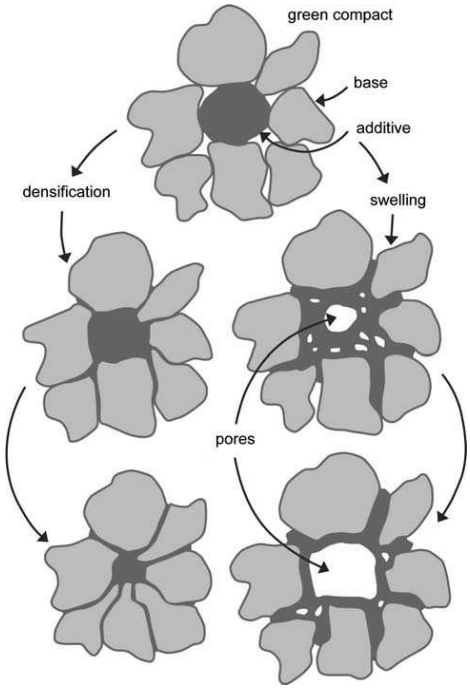

Figure 3.2: The sketch of the microstructural change after melt formation, swelling or shrinkage (re-printed from (German 1985)).

The melt penetrates into the interparticle boundaries and exert capillary force on the wetted surfaces. The magnitude of the capillary force determines the extent of rearrangement, particularly in case of insoluble systems. This force depends upon the contact angle, particle size and amount of the liquid. In general, the amount of the liquid is proportional to the degree of rearrangement; around 30 to 35 volume percent liquid full densification can be achieved by rearrangement and at lower liquid fraction less rearrangement is expected (German (1985)). The smaller particle size enhances the degree of rearrangement and gives densification. Fig. 3.3 shows the effect of particle size in the densification during rearrangement for Fe-Cu system. The initial densification is higher for the smaller Fe particle size and becomes negligible for the Fe particle size of 33 μm. It is reported (Evdokimov *et al.* (1972)) that the capillary force varies inversely to the particle size. Low contact angle favors penetration of the liquid phase between the particles, thus high degree of rearrangement is expected. However, for higher compaction pressure and green density the melt penetration cause swelling during rearrangement because of particle separation. Fig. 3.4 shows that the increase in the compaction pressure inversely effect the densification of the compact.

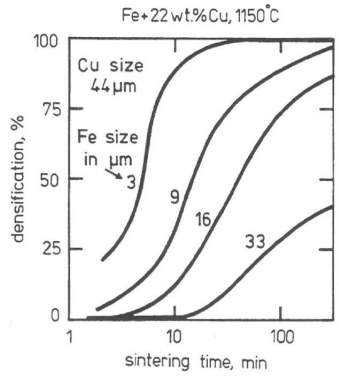

Figure 3.3: The effect of Fe particle size on the densification during rearrangement stage of liquid phase sintering of Fe-Cu compact (re-printed from (German 1985)).

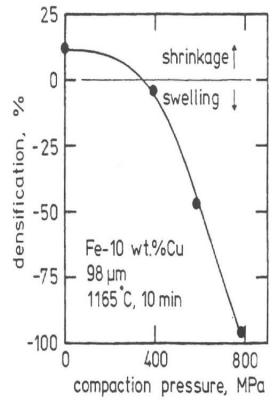

Figure 3.4: The effect of compaction pressure on the dimensional behavior of Fe-Cu compact (re-printed from (German 1985)).

The initial stage sintering behavior of Fe-Cu (-C) is studied extensively (Berner *et al.* (1974), James (1985), Oro *et al.* (2012), (Pelzel (1955), Bocksteigel (1959), Jamil *et al.* (1985), Danninger (1992) are among others)). The mechanism of liquid phase distribution and the subsequent swelling is shown in Fig. 3.5. First, the molten Cu penetrates into the interparticle boundaries and separates them and then the grain boundaries are filled by the liquid phase. The swelling is caused by both particle and grain boundary penetration. The important factors that govern the swelling are green density, amount of Cu, particle size, internal powder porosity and amount of carbon. The effect of solid-state diffusion into Fe on swelling is not important during the initial stage of sintering (Petzow *et al.* (1980)).

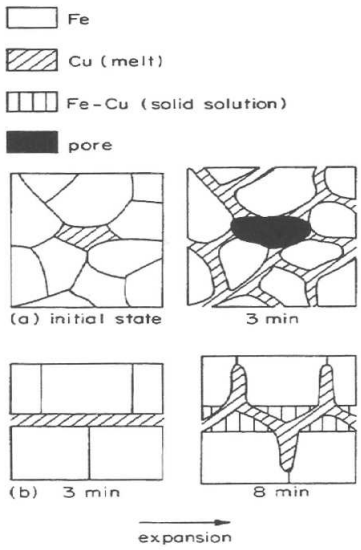

Figure 3.5: Mechanism of swelling; a) particle separation, b) grain boundary penetration (re-printed from (Kaysser *et al.* 1984)).

CHAPTER 4

Basic theory

4.1. Wetting

4.1.1. *Surface tension*

The surface tension can be described as force per unit length or a surface free energy (Probstein (2003), Adamson (1990)). The origin of the surface tension can be traced down to the intermolecular reorganization at the interface between the two phases. A molecule in the bulk liquid is attracted by its neighboring molecules, and the attraction forces are balanced in all directions as shown in Fig. 4.1. While, at the surface (interface), the inward attraction is not balanced by the outward attraction, since there are not so many molecules in the gas phase. This unbalanced attraction will cause a tension on the surface, named as surface tension. Surface tension or surface free energy are interchangeable, and stems from the imbalance of the forces at the interface. The fact that the system always wants to minimize its overall energy results in the contraction of the exposed surface area, so that the unbalanced force at the surface can be minimized. The effect of surface energy is evident in many fields such as coating, soldering, adhesive preparation and sintering of PM steels. The unit of surface energy is force per unit length, or equivalently energy per unit area. The magnitude of surface energy between liquid-vapor phase varies i.e., 0.072 J/m^2 for water-vapor at 20^{o}C and usually more than 1 J/m^2 for high temperature liquid metals.

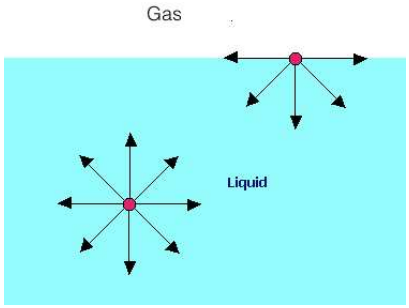

Figure 4.1: Illustrative sketch of the forces acting on a molecule with in the bulk liquid and at the interface (re-printed from (msubbu.in 2014)).

4.1.2. *Wetting and Young-Laplace law*

In a situation when the two fluid phases, for instance liquid-gas, makes a contact with the solid surface, wetting is observed. The meeting point of the three phases is called the three-phase point and in a three dimensional case it will be a line, *contact line* (Fig. 4.2). The surface energies of the interfaces are related to the equilibrium contact angle by the well known Young's equation (Young (1805)). Where σ represents the surface energy of the interface, and subscript denotes the type of interface; S solid, L liquid, and M medium (vapor or gas).

$$cos\theta_e = \frac{\sigma_{SM} - \sigma_{SL}}{\sigma_{LM}} \tag{4.1}$$

The equilibrium angle θ_e is defined as the angle between the tangent along the liquid-vapor interface and the solid surface. θ_e is used to measure the wettability of the liquid, if the angle is less then 90^o the solid is hydrophilic and good wetting is expected. In case of θ_e greater then 90^o, the solid is hydrophobic and wetting is poor. Another measure is the spreading coefficient S, defined as $= \sigma_{SV} - (\sigma_{SL} + \sigma_{LV})$. If S ≥ 0 the liquid spreads completely on the solid surface and if S < 0 partially wetting is observed. High energy surfaces such as metals has higher σ_{SV}, thus good wetting is observed in metallic systems.

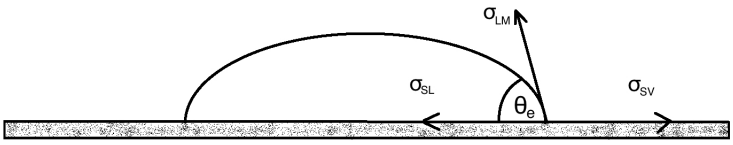

Figure 4.2: Wetting of a liquid drop on a solid surface and surface energies of the interfaces (author's illustration).

The relationship between the surface tension and the interface curvature is given by Young and Laplace (de Gennes *et al.* (1985)). The Young-Laplace law for a spherical drop is shown in Eq. 4.2.

$$P_i - P_o = \Delta P = 2\sigma/R \tag{4.2}$$

Here, P_i is the inside pressure of the drop, P_o is the outside pressure, and R is the drop radius.

4.1.3. *Dynamic wetting*

During wetting of a liquid drop on the solid surface, the contact angle will continuously evolve to achieve its equilibrium value. Extensive (Zisman (1964), Hoffman (1975), de Gennes (1985), Blake (1993), Bonn *et al.* (2009), Leger *et al.* (2011)) work has been

done to explain the evolution of contact angle during wetting. Dynamic wetting can be explained primarily by two theories, known as the molecular-kinetic (MK) theory and the hydrodynamic theory. According to the MK theory (Cherry *et al.* (1969), Blake *et al.* (1969), Blake *et al.* (2002), Carlson *et al.* (2009), Carlson *et al.* (2102)) during wetting the solid substrate offers adsorptive sites for the molecules of the liquid phase. Let k_o and k represent the frequency and length respectively, of each molecular displacement to and from adsorptive sites on the solid surface. Then the velocity of the contact line is determined by the overall molecular displacement, guided by the surface energy, in a preferred direction. Hence, the available energy is dissipated in the TPZ (three phase zone) because of the to-and-fro molecular jumping at the adsorptive sites. However, the hydrodynamic theory emphasizes that the dominant dissipation channel is viscous flow in the wedge-shaped region of the liquid near the TPZ. Despite the fundamental difference in approach, these two theories have been applied successfully for many different systems, implying that, in a broader scenario, both viscous dissipation and contact line friction control the dynamic wetting.

Understanding the wetting process in metals is challenging compared to liquids at room temperature, because of high melting temperatures and possible dissolution effects. This process has been studied by many researchers (Ambrose *et al.* (1993), Saiz *et al.* (2004), Eustathopoulos (2005), Villanueva *et al.* (2009), Kozlova et al. (2010), Dezellus *et al.* (2010), Oro *et al.* (2012), Tahir *et al.* (2013) and more) in order to explain the kinetics of spreading, and how it is affected by the reactivity of the substrate. Generally, wetting is improved by the dissolution of the substrate, but the kinetics of process slows down. In reactive wetting, the first stage of wetting is very fast and diffusion effects are negligible but during the second stage, substrate dissolution becomes active and slow down the speed of liquid front.

4.2. Solid particle rearrangement

Solid particles connected by a liquid bridge can rearrange themselves under the action of capillary pressure. These forces are caused by the surface energies at the solid-liquid-vapor boundary and the pressure difference due to the curved liquid-vapor interface. The initial densification is mainly achieved by the rearrangement of solid particles under the action of capillarity, especially in insoluble systems. Depending upon the contact angle, solid particle separation and the amount of liquid; the capillary forces might be attractive (densification) or repulsive (swelling). Usually for low contact angles ($\approx 0^o$) the attractive forces exerted by the wetting liquid tend to rearrange the solid particles for maximum packing, while for higher contact angle the forces are repulsive and swelling occurs. However, high green density (compaction pressure) might result in the separation of particle (swelling) due to the penetration of liquid phase under the action of capillarity.

Several researchers (Heady *et al.* (1970), Huppmann *et al.* (1975), Anestiev *et al.* (1999)) have reported the theoretical and analytical description of the particle movement connected by the liquid bridge. The theoretical work about the densification during liquid phase sintering proposed that the densification rate is a function of time, temperature, and particle size. Huppmann & Riegger derived the interparticle force as a function of interparticle distance. They also compared the analytical and experimental results performed on tungsten spheres coated with copper.

4.3. Diffusion

The transfer of atoms, either within a solid, or from another phase into solid, is the basic mechanism of sintering. This migration of atoms through the crystal lattice is called *diffusion*. In metals the important diffusion mechanisms are vacancy and interstitial diffusion. Vacancy or substitutional diffusion refers to the atomic jump from its lattice position into an adjacent vacant site. Since the diffusing atoms and vacancies exchange sites, the atomic flux is in the opposite direction of the vacancy flux. In case of interstitial diffusion an atom jumps from an interstitial position to an empty adjacent position. The atoms of relatively small dimensions usually diffuse by this diffusion mechanism such as C, H etc. Fig. 4.3 shows the schematic of the interstitial and substitutional diffusion mechanism. Usually, interstitial diffusion is faster than the substitutional diffusion because of smaller size of interstitial atoms and also that the number of the interstitial sites are larger than the vacant lattice sites.

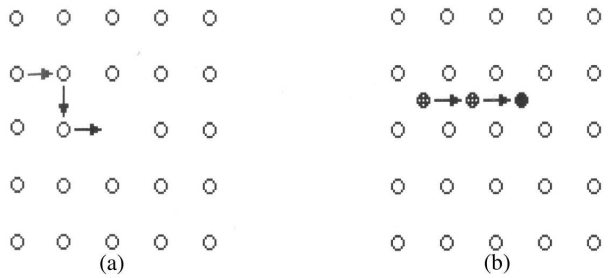

Figure 4.3: Schematic of diffusion mechanism; a) vacancy, b) interstitial, (re-printed from (Höganäs Handbook - 6)).

The difference in concentrations of system components throughout the material is minimized by the movement of atoms. In case of non-steady state diffusion condition, which is the case in many particle situations, the diffusion is described by the Fick's second law of diffusion (Eq. 4.3).

$$\frac{\partial c}{\partial t} = D\frac{\partial^2 c}{\partial^2 x} \tag{4.3}$$

Here, D is the diffusion coefficient, x is the distance, c is the concentration, and t is the time.

CHAPTER 5

Modeling and experiments

5.1. Modeling

5.1.1. *Wetting*

Wetting can be modeled as a free interface problem where the surface energy of the deformable interface between two immiscible fluids can be minimized by the change in their shapes. Several modeling techniques are developed to model the two–phase flow by treating the interface in different ways. Most common are the front-tracking (Unverdi *et al.* (1992)), volume-of-fluid (Hirt *et al.* (1981)), level set (Sussman *et al.* (1994)), and diffuse-interface (phase field method) (Jacqmin (1999)). In addition, molecular dynamics simulations are also used to study the wetting dynamics (Yang *et al.* (1991), Coninck *et al.* (1995), Fan *et al.* (1995), Jin *et al.* (1997)).

In the front-tracking method evenly distributed Lagrangian markers are used to track an interface. The advection of the markers is governed by the velocity field defined on a Eulerian grid. The level set method use a signed distance function to define the interface. The clustering of markers and contours take place in front-tracking and level set method respectively, which is solved by inserting or deleting the markers and by reinitializing the interface. The level set method has been applied to the moving contact line problem (Singh *et al.* (2005), Mukherjee *et al.* (2007), Lesage *et al.* (2007), Son *et al.* (2007)). While, the volume-of-fluid method use a color function to illustrate the shape and evolution of the interface. One common thing in these models is that the boundary condition for the moving liquid front is not well defined.

In the remaining sections, the focus will be placed on the diffuse-interface models. Phase field models for two–phase flow are developed by postulating the free energy of the system. The change in the free energy of system can be used to model the interfacial dynamics by using an appropriate boundary condition. The phase field model, considers that the interface have a finite thickness endowed with physical properties for instance surface tension. In the phase field method, the boundary condition for the contact line motion is derived from the interfacial surface energies, which allows the contact line to move, even with a no-slip condition of the velocity.

The main advantages of the phase field models are, mass conservation, contact line motion, flexibility in simulating 2D, axisymmetric, and 3D problems. However, the finite thickness of the diffuse interface is the major drawback of this method. For instance, a millimeter-sized drop is simulated with the interface thickness ($\sim$ 0.01 mm), which is many fold thicker than the real situation. Even with this unphysical interface thickness, many researcher have used the phase field models to predict the

wetting in accordance with the hydrodynamic theory (Villanueva *et al.* (2006), Yue *et al.* (2010) and Yue *et al.* (2011)).

The two common phase field models are the Cahn-Hilliard and Cahn-Allen theory. Cahn-Hilliard model, uses the conserved order parameter and applies to problems such as, spinodal decomposition, contact-line dynamics, microfluidics applications (Cahn (1961), Badalassi *et al.* (2003), Kim *et al.* (2004)). While Cahn-Allen, uses the non-conserved order parameter and has been applied to problems such as, solidification and nucleation (Boettinger *et al.* (2002), Loginova *et al.* (2003)). The stress singularity for the moving contact line is no longer present due to mass transfer across the interface (Seppecher (1996)). In the above mentioned work, an assumption is made that the moving interface is at local equilibrium during dynamic wetting. It has been shown previously (Carlson *et al.* (2010)) and also in this work (Tahir *et al.* (2013)), that this assumption over predicts the wetting speed and fails to accurately capture the temporal evolution of the contact line. Villanueva *et al.* (2009) qualitatively investigated the important phenomenon in LPS; wetting, microstructure changes, particle motion under capillarity, coalescence and pore elimination using idealized material systems.

5.1.1.1. *Cahn-Hilliard and Navier-Stokes*

The Cahn-Hilliard equation for an iso-thermal, viscous and incompressible binary fluid is derived from the postulate of the system free energy and given in Eq. 5.1 (van der Waals 1893, Cahn 1961). Consider the binary fluid has two components A and B, characterized by an order parameter C, by fixing the value of C in component A as $C_A = 1$ and in component B as C_B = -1.

$$\mathcal{F} = \int_{\Omega} \left(\beta \Psi \left(C \right) + \frac{1}{2} \alpha \left(\nabla C \right)^2 \right) d\Omega + \int_{\partial\Omega} \left[\sigma_{SL} + \left(\sigma_{SV} - \sigma_{SL} \right) g(C) \right] dS \qquad (5.1)$$

The first term on the right hand side of Eqn. 5.1 represents the volume integral over the bulk (Ω) , while the second term gives the boundary integral, including the free energy contribution of the solid substrate ($\partial\Omega$). The two stable phases, A (liquid) and B (Vapor), are described by the two minima of a double-well positive function Ψ. A simplistic example of a double-well function is (C+1)^2(C-1)^2 and this function gives two minima i.e., +1 for liquid and -1 for the vapor phase. The surface tension σ and interface thickness ϵ are controlled by the phase field parameters alpha (α) and beta (β), respectively. The relationship between the phase field parameters and the surface tension and interface thickness are given as, $\alpha = \sigma\epsilon\frac{3}{2\sqrt{2}}$ and $\beta = \frac{3\sigma}{2\sqrt{2\epsilon}}$. The interfacial energies for solid-liquid and solid-vapor are denoted as σ_{ij}, where subscript denote the phases. The free energy formulation at the solid surface is made by taking the integral of the local surface energy, over the solid surface ($\partial\Omega$). The polynomial $g(C) = 0.75C$-$0.25C^3$ is the local surface energy function and varies smoothly from 0 ($C = 1$) to 1 (C = -1). It governs the change in the surface energy with respect to the concentration. The function $g(C)$ is set in such a way that the equilibrium contact angle will evolve according to Young's law.

The variational derivative of the Eqn. 5.1 with respect to the C and subsequent integration by parts yields:

$$\delta F = \int_{\Omega} \{\beta \Psi^{'}(C) - \alpha \nabla^2 C\} \delta C d\Omega + \int_{\partial\Omega} \{\alpha \nabla C.\mathbf{n} + (\sigma_{sv} - \sigma_{sl}) g^{'}(C)\} \delta C dS, \quad (5.2)$$

$\mathbf{n}$ is the surface normal. The first term on the right hand side gives the volume integral of variation of the bulk chemical potential and the second term, defines the boundary integral of the wetting boundary condition. The similar idea was first proposed by Van der Waals, and later Cahn extended the model to time-dependent problems (Cahn (1961)) by assuming that the diffusive flux is proportional to the chemical potential gradients. The Cahn-Hilliard equation, which for the fluid motion is written as,

$$\frac{\partial C}{\partial t} + (\mathbf{u}.\nabla)C = \kappa \nabla^2 \left(\beta \Psi'(C) - \alpha \nabla^2 C\right) \quad \text{in } \Omega, \quad (5.3)$$

where κ is the mobility that is considered to be constant. The dimensionless form of the Cahn-Hilliard equation is shown in Eqn. 5.4,

$$\frac{\partial C}{\partial t} + (\mathbf{u}.\nabla)C = \frac{1}{Pe} \nabla^2 \left(\Psi'(C) - (Cn)^2 \nabla^2 C\right) = \frac{1}{Pe} \nabla^2(\phi), \quad (5.4)$$

The chemical potential (ϕ) is the rate of change of system free energy with respect to C. The Peclet number ($Pe = \frac{2\sqrt{2} L_c U_c \epsilon}{3\kappa\sigma_{lv}}$) is defined as the ratio between the convective and diffusive mass transport.

The term in the boundary integral, see Eqn. 5.2, sets the wetting boundary condition for the liquid-vapor interface right at the solid (wall). By assuming that the liquid-vapor interface is at local equilibrium as it wets the solid surface, the wetting boundary condition becomes as given in Eqn. 5.5. While in case of local non-equilibrium of the liquid-vapor interface right at the solid surface (wall), the wetting boundary condition becomes as shown in Eqn. 5.6. The non-zero value on the left hand side of Eqn. 5.6 allows the contact angle to continuously relax towards equilibrium value. μ_f is defined as the friction parameter between the solid and the liquid at the contact line.

$$0 = \alpha \nabla C.\mathbf{n} + \sigma cos(\theta_e) g^{'}(C) \quad (5.5)$$

$$\epsilon \mu_f \frac{\partial C}{\partial t} = \epsilon \alpha \nabla C.\mathbf{n} + \sigma cos(\theta_e) g'(C) \quad (5.6)$$

The dimensionless Navier-Stokes equations coupled with phase dependent surface tension, for an incompressible binary system are shown in Eqn. 5.7 and Eqn. 5.8. The dimensionless physical parameters, Reynolds number (Re), Weber number (We) and Cahn number (Cn) are shown in Eqn. 5.9. The properties of the liquid (subscript l) are used as reference for the non-dimensionalization of Navier-Stokes equations.

$$\frac{\partial \mathbf{u}}{\partial t} + (\mathbf{u}.\nabla)\mathbf{u} = -\nabla p + \frac{\nabla^2 \mathbf{u}}{Re} - \frac{1}{We.Cn} C \nabla \phi \quad (5.7)$$

$$\nabla.\mathbf{u} = 0 \quad (5.8)$$

$$Re = \frac{\rho_l U_c L_c}{\mu_l},\ We = \frac{2\sqrt{2}\rho_l L_c U_c^2}{3\sigma},\ Cn = \frac{\epsilon}{L_c} \tag{5.9}$$

L_c is the characteristic length, liquid drop diameter, $\mathbf{u}$ is the velocity field, U_c is the characteristic velocity, ρ_l is the liquid density and μ_l is the liquid viscosity. C is a phase field variable, which changes from 1 to -1 in liquid to vapor phase respectively. The transition of C from maximum (1) to minimum (-1), which is rapid but smooth, makes the interfacial region. The phase dependent surface energies are represented by the term $C\nabla\phi$, where ϕ is the chemical potential (Jacqmin (1999)). The Reynolds number gives the ratio between the inertial and the viscous forces. The Weber number is the ratio between inertia and the surface tension force. The Cahn number (Cn) gives the ratio between the interface thickness ϵ and the characteristic length L_c.

In order to model the particle movement under the action of capillarity, the contribution of the capillary force is added in the Navier-Stokes equations as shown in Eq. 5.10. F_{st} is the force exerted by the solid particles on the wetting liquid. The governing equation used to model the displacement of the solid particles is given as in Eq. 5.11.

$$\frac{\partial \mathbf{u}}{\partial t} + (\mathbf{u}.\nabla)\mathbf{u} = -\nabla p + \frac{\nabla^2 \mathbf{u}}{Re} - \frac{1}{We.Cn} C\nabla\phi + F_{st} \tag{5.10}$$

$$\rho_s \frac{\partial^2 \mathbf{u}_s}{\partial t^2} - \nabla \cdot \varsigma = \mathbf{F}_v \tag{5.11}$$

where ρ_s is density of the solid particle, $\mathbf{u}_s$ represents the displacement field, $\mathbf{F}_v$ is the force per unit volume exerted by the wetting liquid, and ς is the elastic stress. Arbitrary Lagrangian Eulerian (ALE) method was used to track the particle displacement.

5.1.1.2. *Numerical treatment*

The finite element method is originated in the field of structural mechanics and now, gaining popularity in solving flow problems especially with complicated geometries (Gresho *et al.* (1998)). The Galerkin finite element method finds weak solutions of a partial differential equations (PDE) by using a piecewise polynomial approximation in space, time, or space/time. The general steps for setting up the weak/variational form are; multiply the PDE with a test function followed by the integration over the entire domain. Integration by parts is applied where required and appropriate function spaces are used. Galerkin finite element method is used for the discretization of the coupled Cahn-Hilliard and Navier-Stokes equations. Homogeneous dirichlet boundary condition is assumed for the velocity, and continuous piecewise linear functions are used. In this work, the treatment of the Navier-Stokes is similar to those of (Hansbo *et al.* (1990)) without the streamline diffusion method. The detailed discussions on the finite element analysis of the Cahn-Hilliard and Navier-Stokes equations can be found (Elliott *et al.* (1992), Barrett *et al.* (1995) (1999), Garcke *et al.* (2001), Barrett *et al.* (2002)). For a general numerical treatment of PDEs, please refer to the previous work (Eriksson *et al.* (1996), Debnath *et al.* (1999), Evans (1998)). A brief summary is given in the following part.

The projection method (Gresho *et al.* (1998), Guermond *et al.* (2006)) is used to solve the Navier-Stokes equations. The decoupled equations for the velocity and pressure are solved at each time. The pressure is treated explicitly at the viscous step and then corrected at the projection step. The first step is to consider the advection-diffusion equation. Moreover, a stabilization term for pressure can be used in projection step to improve stability.

$$\rho\frac{\mathbf{u}^{n+1}-\hat{\mathbf{u}}^{n}}{k_{n+1}}+\rho\mathbf{u}^{n}.\nabla\mathbf{u}^{n+1}-\mu\nabla^{2}\mathbf{u}^{n+1}+\nabla p^{n}=F^{n+1} \tag{5.12}$$

and the projection step is,

$$\rho\frac{\hat{\mathbf{u}}^{n+1}-\mathbf{u}^{n+1}}{k_{n+1}}+\nabla(p^{n+1}-p^{n})=0, \tag{5.13}$$

$$\nabla.\hat{\mathbf{u}}^{n+1}=0. \tag{5.14}$$

Taking $\nabla.$ of Eq. 5.13, Poisson equation for the pressure is formed,

$$\nabla^{2}(p^{n+1}-p^{n})=\frac{\rho}{k_{n+1}}\nabla.\mathbf{u}^{n+1}. \tag{5.15}$$

and the viscous step is,

$$\rho\frac{\mathbf{u}^{n+1}-\mathbf{u}^{n}}{k_{n+1}}+\rho\mathbf{u}^{n}.\nabla\mathbf{u}^{n+1}-\mu\nabla^{2}\mathbf{u}^{n+1}+\nabla(2p^{n}-p^{n-1)}=F^{n+1}. \tag{5.16}$$

The next step is to solve the corresponding discrete system of algebraic equations. A finite linear system of algebraic equations can be solved either by direct methods or iterative methods. For dense matrices (with few zeros), direct methods are preferred. While for sparse matrices, iterative methods such as the generalized minimum residual method (GMRES), conjugate gradient method (CG), multigrid method are generally used (for further reading, see Saad (1996)). The numerical error using the finite element method has the following reasons: (1) the solution is approximated by piecewise polynomials, (2) numerical quadrature error because of evaluating the integrals, (3) solution of the discrete problem, from solving the resulting discrete systems only approximately. For more details, see (Eriksson *et al.* (1995)).

5.1.2. *Diffusion*

After melt formation, the liquid phase penetrates into the interparticle and grain boundaries of the solid structure. Which results in the coating of solid particles with the liquid layer. Hence, for the diffusion calculation a smooth layer of the liquid is assumed at the solid surface. The thickness of the liquid layer is approximated by the weight percentage of the liquid forming additive; if the weight percentage of the liquid forming alloying element is 2% (mass), then the thickness of liquid layer is set to be 2% of the total cell width. It is observed (Tahir *et al.* (2014)) that the solid-state diffusion of the alloying elements (except C) becomes significant after melting and subsequent coating of the solid particle by the liquid phase. So the starting point of the temperature cycle used for the diffusion calculations is set to be above the melting point of the liquid forming alloying element (i.e., Cu). DICTRA (Höglund

et al. 2002) simulations for the diffusion of alloying element in the base powder were performed using the Thermo-Calc software TCFE6 Steels/Fe-alloys database (2013) and DICTRA mobility database mob2 (2013).

5.2. Experiments

5.2.1. *Materials*

The powder mixes investigated were Fe-2Cu, Fe-2Cu-0.5C and Fe-2MA-0.5C. MA is the Cu based master alloy containing small amount of the Ni and Si. The detail of powder mixes composition and types of powders used are given in Table. 5.1. The elemental powders were mixed in case of Fe-2Cu(-C) system, and for the master alloy system Cu is pre-alloyed with Ni and Si and then mixed with the Fe base powder.

Composition	Powder specification
Fe-2%Cu-0.6%lubricant	Fe, Höganäs powder grade ASC100.29
Fe-2%Cu-0.5%C-0.6%lubricant	Cu, electrolytic -325 mesh
Fe-2%MA-0.5%C-0.6%lubricant	C, graphite powder, Kropfmühl UF4
MA = Cu-2%Ni-1.5%Si	MA, water-atomized powder -45 μm

Table 5.1: Powder mixes composition and types of powders.

The test specimens from the powder mixes were prepared by conventional uniaxial compaction. The compaction pressure of 600 MPa was applied to achieve a green density of approximately 7 g/cm^3. Cylindrical shaped specimens (diameter = 6 mm, height = 12 mm) were prepared for the subsequent investigations. The lubricant used was 0.6% Kenolube and dewaxing was performed in a laboratory batch furnace at 600^{o}C for 30 min in an atmosphere of 75 vol.-%H2–25 vol.-%N2.

5.2.2. *Sintering trials and dilatometry*

The interrupted sintering trials were carried out in a "Theta" 1600 vertical differential pushrod dilatometer. The principle of the differential (dual rod) dilatometry is based on measuring the difference in dimensional change between a test specimen and a standard material. In this way high accuracy of ∼0,000125 mm is achieved for studying the dimensional evolution of materials. The dimensional changes of the test specimen can be associated with the events such as thermal expansion, phase change, liquid phase penetration and densification. A cylindrical shaped specimen of Al_2O_3 is used as a reference. The dilatometer is equipped with a SiC heating element furnace which can reach temperatures up to 1550°C while applying heating rates up to 70 K/min and has the capability for fast cooling (100-150 K/min).

The atmosphere used for the interrupted sintering trials was 90 vol.-%N2–10 vol.-%H2 and the gas flow was 1 lt./min. Multiple sintered samples were prepared for each material system by varying the maximum temperature and isothermal holding times at 1120^{o}C. All the sintering trials were performed with the heating rate of 1 ^{o}C/s from RT to 800^{o}C and 0.4 ^{o}C/s from 800^{o}C to 1120^{o}C, while the cooling rate from 1120^{o}C to RT was set to be 5 ^{o}C/s.

5.2.3. *Microscopy*

Light optical microscopy (LOM) was used to study the microstructural evolution during the sintering cycle. The cross-sections of the specimens were prepared by cutting, grinding and polishing. The specimens were subsequently etched with pikral/nital prior to LOM. The behavior of liquid phase in term of melting and penetration into solid matrix is investigated. Moreover, the kinetics of liquid phase penetration and subsequent dissolution in the base powder is studied. In addition, the change in the total porosity during sintering is investigated for the Fe-2%Cu (-C) system.

Energy dispersive X-ray spectroscopy (EDXS) is performed to measure the Cu diffusion in Fe, at Fe interparticle boundaries during sintering. The diffusion measurements were carried out using a Hitachi 3700N equipped with the Quantax system. The samples were etched with 1% nital to be able to identify Cu-rich Fe interparticle boundaries, before performing line scans. The accelerating voltage was set to 15 kV and the working distance was 10 mm. The minimum detectable composition was assumed to be 0.3% mass. It is difficult to find a representative measure of the diffusion distance of alloying element in sintered cross section; irregular powder shapes, possible contact of the base particle with the additive particle or not, and the position of the section makes it challenging. That is why multiple line scans were performed on each sample to measure the alloying element (Cu) diffusion distance in Fe. The measured concentration profiles were fitted to a bell curve to extract the diffusion distance (refer Paper 3 and 4 in part II).

CHAPTER 6

Summary of results

6.1. Wetting

Phase field simulations were performed to simulate the wetting of molten metals on solid surfaces. The numerical model is implemented to predict the dynamic wetting of millimeter-sized metallic drops and subsequently verified with the experimental results. After this, the model is applied to predict the dynamic wetting of the micrometer-sized metallic drop. The metallic systems investigated were Cu on Mo, Cu + 3%Fe on Fe + 8%Cu, and Cu on Fe. Realistic physical properties (density, viscosity) and wetting parameters (equilibrium contact angle, drop diameter) were given as input to model. Some representative 3D snapshots of the wetting simulations are shown in Fig. 6.1. The initial condition of simulations is shown in the snapshot at $t = 0$. The evolution of the dynamic contact angle as the wetting progresses is shown in the snapshot at $t > 0$.

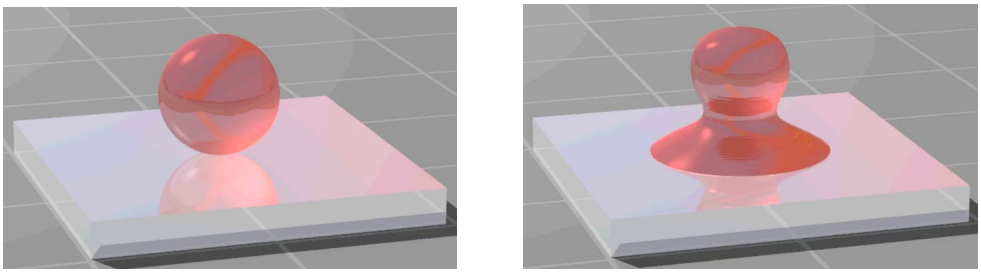

(a) (b)

Figure 6.1: 3D snapshot sequence of wetting simulations: (a) at $t = 0$, (b) $t > 0$. The time for the snapshots is in dimensionless form. Fig. 2 in Paper 1 in Part II.

The values of Reynolds number (Re), Peclet number (Pe), and the Cahn number (Cn) are 200, 10^3, and 0.01 respectively. Since inertia regulates the wetting in high density and surface energy metals, the characteristic speed is calculated using inertial scaling. Figure. 6.2 shows the temporal evolution of drop base radius of a millimeter-sized Cu drop progressively wetting the Mo substrate. The simulation with only viscous dissipation near the vicinity of contact line region, over predicts the liquid frond speed and match with the experiments is obtained by including the friction dissipation at the contact line. Non-equilibrium boundary condition ($\mu_f > 0$) is used to introduce the friction parameter, μ_f, in the model to accommodate the energy dissipation because of contact line friction. In case of Cu on Mo the predicted value

of the adjustable friction parameter, μ_f is 6.12 Pa.s for $\theta_e = 26^o$, and for saturated compositions of Cu on Fe at $\theta_e = 74^o$, μ_f is 3.4 Pa.s. It is observed that the magnitude of the fitted friction parameter, μ_f, is directly proportional to the wettability of the liquid; higher wettability gives stronger interaction between metallic liquid and the solid substrate resulting in higher value of friction parameter. Moreover, the simulations predict the relaxation of contact angle towards equilibrium value and its relationship with the contact line speed. In accordance with the experimental findings a linear relation between the contact angle and contact line speed, except in the impact regime, is observed.

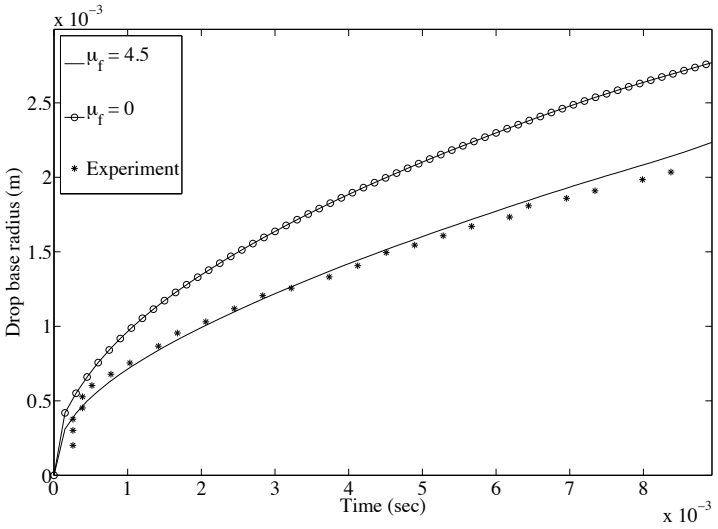

Figure 6.2: Comparison between experimental and simulation results of drop base radius displacement vs. time. The solid line with open symbols shows the simulation results with $\mu_f = 0$. The solid line shows the simulation results with $\mu_f = 4.5$ (dimensional value = 6.12 Pa.s). The experimental results are shown by asterisks. Fig. 5 in Paper 1 in Part II.

Fig. 6.3 illustrates the isocontours of the metal drop shape at different time during wetting. It is found that the change in the boundary condition affects the temporal evolution of dynamic contact angle and surface curvature of wetting metallic drop. The equilibrium boundary condition immediately imposes the contact angle right at the substrate and also allows more surface curvature, thus adding extra speed. In case of non-equilibrium boundary condition the dynamic contact right at the solid surface continuously relax towards the equilibrium value. Qualitatively the pattern of dynamic wetting of a micrometer-sized metal drop is in many ways similar to that of the millimeter-sized. For example, bending of the liquid-vapor interface, propagation of the capillary wave, and the temporal evolution of the liquid front speed. However, the wetting process is much faster at the micro level compare to the millimetric scale. The simulations predict that the wetting speed of a millimeter-sized metal drop is in

the order of 0.1-1 m/s and found to be in the range of 2-20 m/s for the micrometer-sized drop. In addition, the predicted time for the micrometer-sized drop to spread 31μm is 4.9 μs.

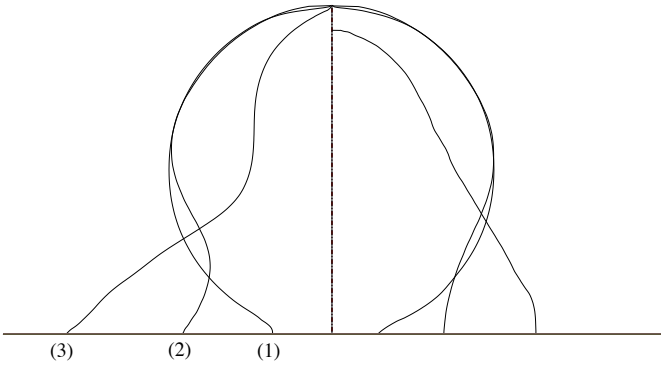

Figure 6.3: Drop shape evolution on both sides of the center line at $t = 0.3$, 2.1 and 6.75 ms, corresponding to marks (1), (2) and (3), respectively. The left hand side of the center line shows simulation results with the equilibrium boundary condition, and the right-hand side shows result with non-equilibrium boundary condition. Fig. 4 in Paper 1 in part II.

6.2. Microstructure

LOM images of the polished and etched cross-sections of sintered samples were investigated to analyze the liquid phase penetration/distribution and change in porosity during sintering. Interrupted sintering trials were performed by using Theta industries dilatometer; multiple sintered samples were prepared for each material system by interrupting the temperature cycle at different points (refer Paper 2, 3 and 4 in part II). The material systems investigated were Fe-2Cu, Fe-2Cu-0.5C and Fe-2MA-0.5C. More details about the powder used and manufacturing parameters are given in Paper 2, 3 and 4.

Fig. 6.4 show the LOM images of Fe-2Cu and Fe-2Cu-0.5C system respectively, sintered for 3 min at 1120^{o}C. C-added sample show thin seams of undissolved Cu between the interparticle boundaries, whereas Cu is completely dissolved in the C-free sample. The distribution of Cu by liquid penetration into interparticle boundaries and the grain boundaries with in the solid particles is achieved in less than 3 min of holding time at 1120^{o}C. Although the effect of C on the interparticle boundary penetration by liquid Cu is not obvious, as the extent of liquid Cu penetration into Fe interparticle boundaries is fairly equal in both systems. But the presence of free Cu in the C-added system clearly suggests that C does hinder or limit the molten Cu distribution. The

effect of C addition is noticeable in case of grain boundary penetration, as liquid Cu is not able to penetrate all the grain boundaries, especially in large Fe particles, in the C-added system (see Fig. 6.4b). The unfilled grain boundaries can be seen in the C-added even after sintering for 33 min at 1120^{o}C (see Fig. 6.5b). The porosity changes of the Fe-2Cu and Fe-2Cu-0.5C compacts during sintering were measured by LOM image analysis.

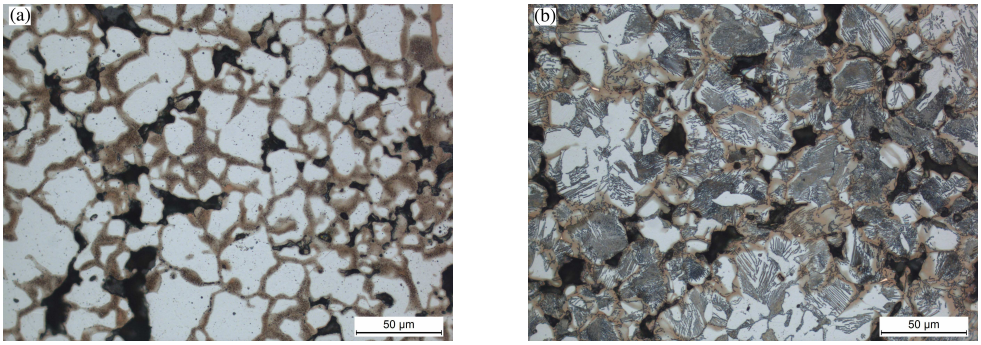

(a) (b)

Figure 6.4: Microstructure of samples after sintering at 1120^{o}C for 3 min: (a) Fe-2Cu, (b) Fe-2Cu-0.5C, pikral etched. Fig. 6 in Paper 3 in part II.

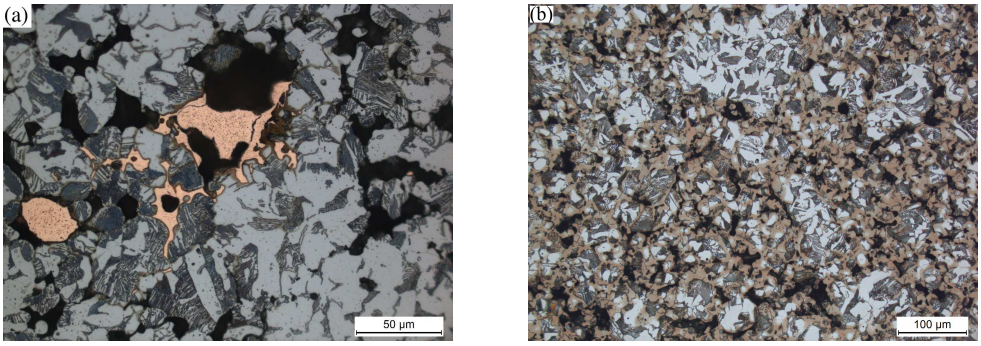

(a) (b)

Figure 6.5: Microstructure of samples: (a) Fe-2MA-0.5C, sintered at 1080^{o}C, pikral etched, (b) Fe-2Cu-0.5C, sintered at 1120^{o}C for 33 min, pikral etched. Fig. 4f and Fig. 5b in Paper 4 and Paper 3 respectively, in part II.

LOM images (see Fig. 6.5a) indicate that in case of the Fe-2MA-0.5C system, the melting behavior of the master alloy is different from the pure Cu where melting occurs at a precise temperature. The master alloy particles melt progressively over a temperature range, which subsequently penetrates into the Fe interparticle and grain boundaries. The penetration into solid network starts at trial 2 (1060^{o}C) and

almost all the Fe interparticle boundaries were penetrated after trial 4 (1090^{o}C). The distribution behavior of master alloy in Fe-2MA-0.5C is similar to that of liquid Cu in Fe-2Cu-0.5C system, where all the interparticle boundaries were penetrated by the liquid phase but the grain boundary penetration was limited especially in the large Fe particles. The thermodynamic calculations also predicted the existence of the two-phase region during melting for the master alloy composition.

6.3. Dimensional variations

The *dilatometry curves* show the dimensional behavior of the specimen during sintering cycle. Fig. 6.6 shows the dimensional changes of the Fe-2Cu and Fe-2Cu-0.5C samples, sintered for 33 min at 1120^{o}C, associated with the thermal expansion, phase change, liquid phase penetration and densification. One interesting feature of the dilatometry curve is the sudden expansion associated with the melting of alloy elements (Cu). The magnitude and slope of this expansion peak can be related with the kinetics and extent of the liquid phase penetration into solid interparticle/grain boundaries. It is observed that there is an expansion jump after the melting point of Cu in the C-free system, while for the C-added system this expansion jump is delayed in time and reduced in magnitude. The comparison between the magnitude of the expansion peak of Fe-2MA-0.5C and Fe-2Cu-0.5C shows that the master alloy system experienced relatively less expansion compared to the Fe-2Cu-0.5C system.

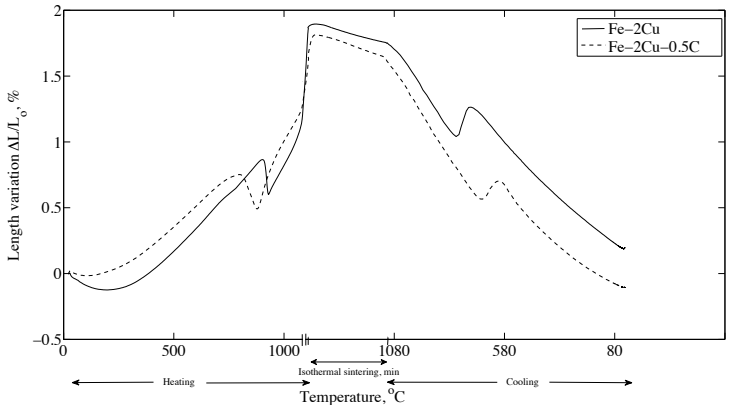

Figure 6.6: Dilatometer curves for Fe-2Cu and Fe-2Cu-0.5C samples, sintered for 33 min at 1120^{o}C (trial 6). Fig. 9 in Paper 3 in part II.

These variations in the expansion magnitude after melting of liquid forming additive can be explained on the basis of alloy element redistribution. The kinetics and extent of liquid phase penetration depend upon wettability, dissolution effects, and melting behavior. The penetration of liquid phase into Fe interparticle and grain boundaries is hindered in Fe-2Cu-0.5C system, either because of increase in the contact angle or the enhance dissolution effects with the C addition, resulting in less and delayed expansion compared to the Fe-2Cu system. In case of the Fe-2MA-0.5C system, the reduced magnitude of the expansion peak in comparison with the Fe-2Cu-0.5C is possibly due to the melting behavior of the liquid forming additive (MA). The

continuous melting of the master alloy particles results in uninterrupted but partial penetration of the liquid phase into solid skeleton contrary to instant melting and complete penetration of liquid phase as in case of pure Cu.

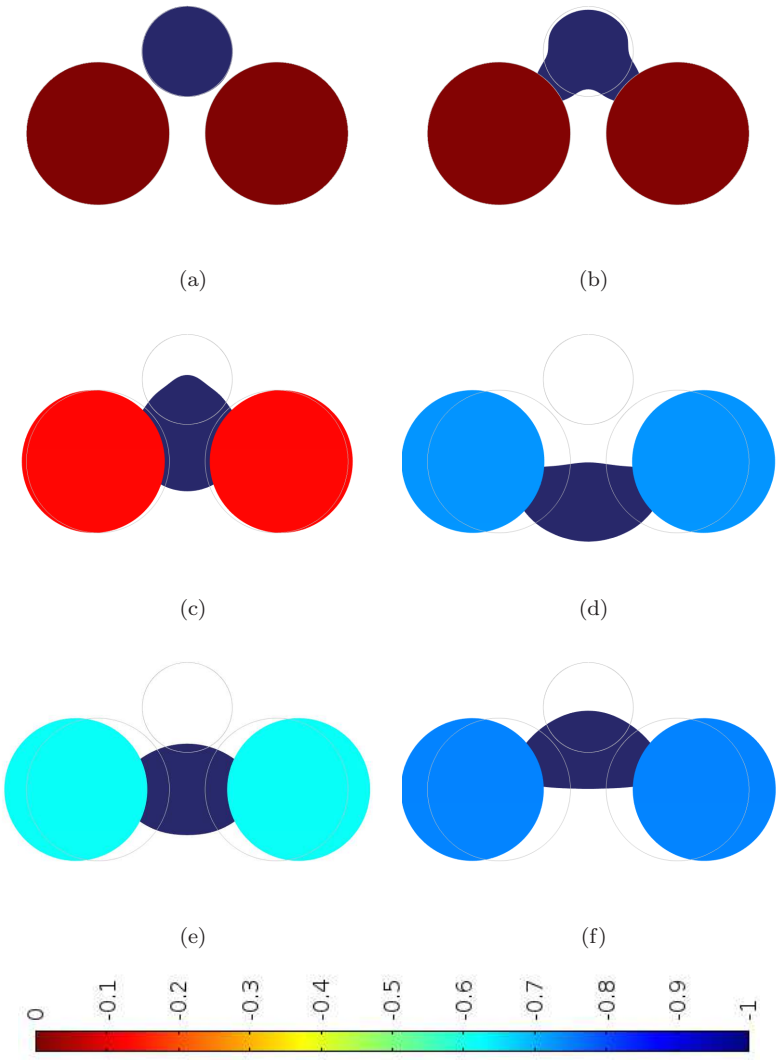

Figure 6.7: Snapshots of particle-motion simulations for liquid phase ratio of 0.2 and contact angle of 100^o: a) 0 ms, b) 4 ms, c) 10 ms, d) 19 ms, e) 32 ms, f) 43 ms. The hollow shapes indicate the initial positions of the solid particles and the liquid drop. The magnitude of the particle movement is indicated by the color bar. Fig. 5 in Paper 5 in part II.

Numerical simulation of the dimensional variations under the action of capillarity during primary rearrangement stage of LPS was performed using COMSOL Multiphysics. Phase field model is used to simulate the wetting/penetration of liquid phase and the consequent motion of the solid particles is modeled by using linear elastic material. The coupling of these two phenomena, wetting and motion of solid particle, was done by fluid-structure interaction (FSI) technique. First, 2D simulation of the liquid penetration into the channel between two solid particles and the motion of solid particles under the action of capillarity is modeled and compared with the analytical approximation. The simulations of the liquid penetration into interparticle channel correctly predict the trend of decrease in the penetration rate of liquid phase with the increase in the equilibrium contact angle for a fixed channel depth of the 100 μm. The simulation results of the solid particle motion connected by a liquid bridge, by varying the contact angle and amount of liquid phase, present good agreement with the analytical estimates. Fig. 6.7 shows the temporal evolution of the solid particle motion connected by a liquid bridge with equilibrium contact angle 100^o and liquid area ratio 0.2.

The magnitude of capillary forces exerted by the wetting liquid depends upon the contact angle, amount of liquid and interparticle distance. The solid particles were pushed away in case of contact angle 90^o and 100^o for the liquid area ratios of 0.1, 0.2. While, the motion of the solid particles was found to be inward (pulled) in case of contact angle of 40^o. A simple model of two solid particles in contact with liquid phase was used to investigate the effect of amount of liquid phase on the extent (magnitude) and nature of particle motion (inward or outward). The amount of liquid phase, area ratio, was varied from 0.05 to 0.2 and the resulting dimensional change was expressed as $\frac{\Delta l}{l_0}$, where $\triangle l$ is difference between the initial distance, l_o, between the centers of the solid particles and the final distance, l_f, after equilibrium. It is found that both shrinkage and expansion can be experienced by keeping the contact angle and compact density (interparticle distance) constant and only varying the amount of liquid phase. The liquid area ratio of 0.05 gives the inward motion of the solid particles (shrinkage), while in case of area ratios 0.1, 0.15, and 0.2 outward motion of the solid particles (swelling) is observed (refer to Paper 5 in part II).

6.4. Diffusion

EDXS analysis was performed to investigate the solid-state diffusion of Cu in Fe, at the Fe interparticle boundaries during sintering. Multiple line scans were performed on each sintered sample to measure the Cu diffusion distance in Fe. The investigations were performed on the sintered samples of the Fe-2Cu, Fe-2Cu-0.5C and Fe-2MA-0.5C systems. In order to extract the diffusion distances, the EDXS measured concentration profile was fitted to the bell curve of the function, $y = a.e^{-(x_d - x_c)/w}$. Where a is the height of the curve's peak, x_c defines the position of the center of the peak, and w controls the width of the curve. The minimum detectable concentration (MDC) of Cu was assumed to be 0.3% (mass). The diffusion analysis shows that the solid-state diffusion of Cu at the Fe interparticle boundaries becomes significant only after the melting point of Cu is reached.

Fig. 6.8 shows the EDXS measured Cu diffusion distances in Fe for different holding times during sintering for the Fe-2Cu and Fe-2Cu-0.5C system. The error bars show a standard deviation of uncertainty around the mean value. In the C-free

system, 65 % of the final (33 min at 1120^{o}C) mean Cu diffusion distance is achieved within 3 min of holding time at 1120^{o}C, compared to the 40 % of the total mean Cu diffusion distance in C-added system. The mean Cu diffusion distance in Fe for trial 3 (3 min at 1120^{o}C) is 3.7 μm and 2.4 μm for C-free and -added system respectively. And the final mean Cu diffusion distances in Fe for trial 6 (33 min at 1120^{o}C) are, almost the same, 5.9 and 6.1 μm for C-free and C-added system respectively. The hindered penetration of the liquid Cu in C-added system delays the availability of molten Cu, which results in lower initial diffusion distances compared to the C-added system, but the pockets of free Cu maintain the supply of Cu and hence the final diffusion distances in both systems are similar. In case of Fe-2MA-0.5C system, Cu diffusion distances in Fe lies in the same range after 34 min of sintering at 1120^{o}C as found in Fe-2Cu-0.5C system. This indicates that the homogenization level of Cu in master alloy system is approximately the same but with reduced expansion peak.

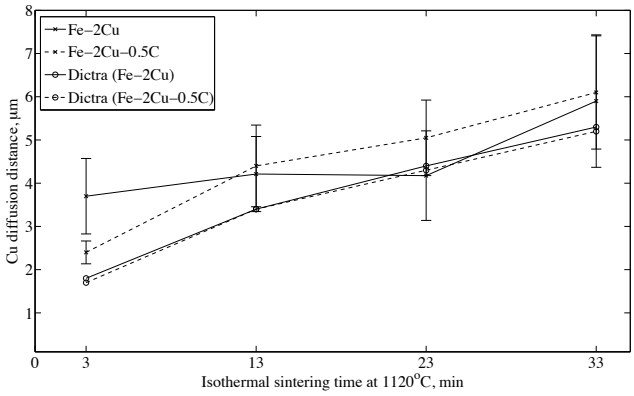

Figure 6.8: Cu diffusion distances in Fe for Fe-2Cu and Fe-2Cu-0.5C systems for holding times of 3, 13, 23, 33 min at 1120^{o}C. The lines with x-marks show the EDXS measured results. The lines with circles show the DICTRA results. Fig. 12 in Paper 3 in part II.

DICTRA simulations were performed to predict the diffusion distances of Cu in Fe and how it is affected by C addition. The predicted diffusion distances for Fe-2Cu and Fe-2Cu-0.5C systems were obtained and plotted as shown in Fig. 6.8. DICTRA simulations show that the diffusion distances of Cu in Fe and Fe-0.5C are equal, which means that the diffusion of Cu in Fe remains unaffected by the C addition. Overall, the predicted diffusion distances match very well with the experimental findings. These results further validate the argument that the lower Cu diffusion distance measured by EDXS in C-added system at trial 3 is the result of hindered Fe interparticle boundary penetration by liquid Cu, which in turn delays the availability of liquid Cu for solid-state diffusion of Cu in Fe.

CHAPTER 7

Conclusions and outlook

An axisymmetric model based on the phase field theory is used to simulate the dynamic wetting of millimeter- and micrometer-sized metallic (Cu) drops. The contribution of energy dissipation because of the contact line friction is introduced to accurately match the experimental results. We predicted the wetting kinetics of the micrometer-sized drop and simulations show that, qualitatively many features of the dynamic wetting of a micrometer-sized metal drop are similar to that of a millimeter-sized drop. A numerical approach is presented to study the primary rearrangement phase of LPS. The simulations predicted the processes such as, wetting/penetration kinetics of liquid phase and motion of solid particles under the action of capillary force, using realistic physical properties, and a qualitative match between the simulation results and the analytical estimates is found.

The quantitative analysis of kinetics of the Cu redistribution showed that the liquid penetration into Fe interparticle/grain boundaries is achieved in less than 3 min of holding time at 1120^{o}C. The C-added systems (Fe-2Cu-0.5C and Fe-2MA-0.5C) show hindered/delayed penetration of the liquid phase in the solid matrix, which results in relatively lower diffusion distances of Cu in Fe. For longer sintering time, the Cu diffusion in Fe was almost similar for all test systems. The master alloy system show least magnitude of expansion peak and we proposed that the melting of liquid forming master alloy particles over a temperature range could be the possible reason.

We observed that modeling the wetting/penetration and consequent particle motion with the phase field method can be a powerful and practical approach. This work successfully model many important processes such as wetting, liquid phase penetration, diffusion, and particle rearrangement during LPS and could be extended for further studies. For instance, modeling the secondary rearrangement stage involving dissolutions, fragmentation and clustering etc. The reactive modeling using realistic physical properties is another exciting and feasible future work. In addition, modeling the rearrangement phase of LPS with realistic geometries (irregular) of the powder particles would be helpful to develop a detailed numerical model. It has been observed that C addition and the melting of the liquid forming phase over a range of temperature slows down the penetration kinetics and consequently reduces the magnitude of volumetric expansion. It would be interesting to further investigate the effect of these parameter by quantifying their individual contribution for the reduction in penetration kinetics and so the volumetric expansion. The combination of experimental techniques (like EDXS) and numerical tools (DICTRA or phase field) could be potentially used for studying the diffusion of the alloying elements in more complex material systems.

Acknowledgment

First and foremost, I am very grateful to THE Almighty Allah for HIS blessings.

I would like to express my sincere gratitude to my supervisor Prof. Gustav Amberg for the continuous support of my PhD study, for his patience, enthusiasm, motivation, and immense knowledge. His ability to explain complex problems in a simple way and always being intuitive, yet rational in approach for making the things work inspired me in all the time of research and writing of this thesis.

I would like to express my gratitude to Dr. Minh Do-Quang for his tremendous guidance and support in numerical modeling. I am truly grateful to Dr. Peter Hedström for his support in experimental investigations, discussion of results and dedication in meticulously examining the manuscripts and thesis. My special thanks to Prof. John Ågren, Prof. Annika Borgenstam, Asst. Prof. Joakim Odqvist for many fruitful discussions and valuable feedback.

The support of Hero-m, financed by VINNOVA, Swedish industry, and KTH Royal Institute of Technology is gratefully acknowledged. My sincere thanks to Ola Bergman (Höganäs AB) and Karin Frisk (Swerea KIMAB AB) for many valuable discussions, sharing their industrial experience and giving important feedback during the project. I would like to thank Heike Grosser (Höganäs AB) for her support in metallography. I also want to thank Dimitris Chasoglou (Swerea KIMAB AB) for performing sintering trials and giving feedback on the manuscript.

I would like to thank the staff, colleagues, and friends at the department of mechanics for their support and providing friendly environment. Many thanks to Timea, Daniel, Zeinab, Dr. Jiewei, Carolina, Heide, Pär Ekstrand, and in particular to Dr. Amer Malik for helping me to reach the finish line.

Finally, a special thank to my parents for their prayers and support throughout my life. I also want to deeply thank my beloved wife, *Alia*, who always prayed for my success and for her endless support during this work. Last but not least, I extend my sweet love to my wonderful children, *Rohaan and Mahad*. Their "cute support" for making sure that I should not work after coming back home is happily acknowledged.

Bibliography

Adamson, A. W.: *Physical chemistry of surfaces*, 5th edn. 1990, New York, John Wiley & Sons, Inc.

Ambrose, J. C.: Ph.D. thesis, Imperial College of Science, Technology and Medicine, 1992.

Angers, R. and Trudel, Y.: *Modern development in powder metallurgy*, Vol. 6. 1974, Princeton, NJ, MPIF.

Ambrose, J. C., Nicholas, M. G. and Stoneham, A. M.: *Acta. Metall. Mater.*, 1992, 40, 2483.

Aksay, I. A.: *J. Phys. Chem-US*, 1974, 78, 1178.

Ambrose, J. C., Nicholas, M. G. and Stoneham A. M.: *Acta Metall. Mater.*, 1993, 41, (8), 2395.

Anestiev, L. A. and Froyen, L.: *J. Appl. Phys.*, 1999, 155, 96.

Bauer, W. and Huppmann, W. J.: *Powder Metall.*, 1975, 8, 249.

Berner, D., Exner, H. E. and Petzow, G.: *Modern development in powder metallurgy*, Vol. 6. 1974, 237.

Bocksteigel, G.: *Stahl Eisen*, 1959, 79, 1187.

Bocksteigel, G.: *Metallurgie III*, 1962, 4, 65.

Blake, T. D.: *Wettability*, Dekker, New York, 1993.

Bonn, D., Eggers, J., Indekeu, J., Menunier, J. and Rolley E.: *Rev. Mod. Phys.*, 2009, 81, 739.

Blake, T. D. and Coninck, J. D.: *Adv. Colloid. Interfac*, 2002, 96, 21.

Blake, T. D. and Haynes, J.: *J. Colloid Interface Sci.*, 1969, 30, 421.

Badalassi, V. E., Ceniceros, H. D. and Banerjee, S.: *J. Comp. Phys.*, 2003, 190, 371.

Boettinger, W. J., Warren, J. A., Beckermann, C. and Karma, A.: *Ann. Rev. Mater. Res.*, 2002, 32, 163.

Barrett, J. W. and Blowey, J. F.: *Numer. Math.*, 1995, 72, 1.

Barrett, J. W. and Blowey, J. F.: *Math. Comp.*, 1999, 68, 487.

Becker, R. and Rannacher, R.: *Acta. Numerica.*, 2001, 10, 1.

Cahn, J. W.: *Acta Metallurgica*, 1961, 9, 795.

Carlson, A., Do-Quang, M. and Amberg G.: *Phys. Fluids*, 2009, 21, 121701.

Carlson, A., Bellani, G. and Amberg G.: *EPL*, 2012, 97, 44004.

Carlson, A., Do-Quang, M. and Amberg G.: *Int. J. Multiphase Flow*, 2010, 36, 397.

Coninck, J. D., D'Ortona, U., Koplik, J. and Banavar, J. R.: *Phys. Rev. Lett.*, 1995, 74, 928.

Cherry, B. and Holmes, C.: *J. Colloid Interface Sci.*, 1969, 29, 174.

Danninger, H.: *Powder Metall. Int.*, 1992, 24, 163.

Danninger, H. and Zengin, O. Z.: *Modern development in powder metallurgy*, Vol. 21. 1988, 171.

Danninger, H.: *Powder Metall. Int.*, 1988, 20, 7.

Danninger, H. and Kara, T.: *Powder Metall. Int.*, 1988, 20, 9.

Danninger, H.: *Powder Metall. Int.*, 1992, 24, (2).

de Gennes, P. G.: *Rev. Mod. Phys.*, 1985, 57, 827.

Dezellus, O. and Eustathopoulos, N.: *J. Mater. Sci.*, 2010, 45, 4256.

Dorweiler, H. J. and Dautzenberg, N.: *Powder Metall. Int.*, 1985, 17, 279.

Durdaller, D.: Höganäs technical bulletin 174D, 1971, 471.

Do-Quang, M. and Amberg, G.: *Int. J. Multiphase Flow*, 2009, 80, 1664.

Debnath, L. and Mikusinski, P.: *Introduction to Hilbert spaces with applications*, 2nd edn., 1999.

Davies, T. J. and Lawcock, R. L.: *Powder Metall.*, 1990, 33, 147.

Eremenko, V. N., Naidich, Y. V. and Lavrinenko, I. A.: *Liquid Phase Sintering*, Consultant Bureau, New York, 1970.

Elliot, J. E.: *Metallurgie*, 1959, 59, 17.

Evdokimov, V. A., Naidich, Y. V. and Lavrinenko, I. A.: *Soviet Powder Met. Metal Ceram.* , 1972. 11, 715.

Eustathopoulos, N., Nicholas, M. G. and Drevet, B.: *Wettability at High Temperatures*, Pergamon, Amsterdam, 1999.

Eustathopoulos, N.: *Curr. Opin. Solid St. M.*, 2005, 9, 152.

Elliott, C. M. and Larsson, S.: *Math. Comp.*, 1992, 58, 603.

Eriksson, K., Estep, D., Hansbo, P. and Johnson, C.: *Acta Numerica.*, 1995, 105.

Eriksson, K., Estep, D., Hansbo, P. and Johnson, C.: *Computational Differential Equations*, Student literature, Lund, Sweden, 1996.

Froschauer, L. and Fulrath, R. M.: *J. Mater. Sci.*, 1976, 11, 142.

Froschauer, L. and Fulrath, R. M.: *J. Mater. Sci.*, 1975, 10, 2146.

Fan, C. F. and Cagin, T.: *J. Chem. Phys.*, 1995, 103, 9053.

Findeisen, G.: *Metall.*, 1960, 14, 295.

German, R. M.: *Powder Metallurgy Science*, Second Edition, Metal Powder Industries Federation, 1994.

German, R. M.: *Powder Metallurgy & Particulate Materials Processing*, Metal Powder Industries Federation, 2005.

German, R. M.: *Liquid Phase Sintering*, Plenum Press, New York, 1985

German, R. M., Zovas, C. Li, P. and Hwang, K. S.: *Progress in powder metallurgy*, Vol. 38, 1982, Princeton, NJ, MPIF.

Garcke H., Rumpf, M. and Weikard, U.: *Interfaces and Free Boundaries*, 2001, 3, 101.

Guermond, J. L. and Quartapelle, L.: *Int. J. Numer. Methods Fluids*, 1998, 26, 1039.

Höganäs Handbook for Sintered Components - 1. Materials and powder properties, Höganäs AB, 1997.

Huppmann, W. J.: *Z. Metallkd*, 1979, 70, 707.

Huppmann, W. J. and Petzow, G.: *Z. Metallkd*, 1976, 67, 579.

Huppmann, W. J.: *Z. Metallkd*, 1979, 70, 792.

Hoffman, R.: *J. Colloid and Interface Science*, 1975, 50, 228.

Heady, R. B. and Cahn, J. W.: *Metallurgical Trans.*, 1970, 1, 185.

Huppmann, W. J. and Riegger, H.: *Acta Metallurgica*, 1975, 23, 965.

Höganäs Handbook for Sintered Components - 6. Metallography, Höganäs AB, 2007.

Hirt, C. W. and Nichols, B. D.: *J. Comp. Phys.*, 1981, 39, 201.

Huh, C.and Scriven, L. E.: *J. Colloid Interface Sci.*, 1971, 35, 85.

Höglund, L., Shi, P. F., Sundman, B., Andersson, J. O. and Helander, T.: *Calphad*, 2002, 26, 273.

Hansbo, P. and Szepessy, A.: *Comput. Meth. Appl. Mech. and Eng.*, 1990, 84, 175.

Huh, C. and Scriven, L. E.: *J. Colloid Interface Sci.*, 1971, 35, 85.

James, B. A.: *Powder Metall.*, 1985, 28, 121.

Jin, W., Koplik, J. and Banavar, J. R.: *Phys. Rev. Lett.*, 1997, 78, 1520.

Jamil, S. J. and Chadwick, G. A.: *Powder Metall.*, 1985, 28, 65.

Kingrey, W. D.: *J. Appl. Phys.*, 1959, 30, 301.

Kozlova, O., Voytovych, R., Protsenko, P. and Eustathopoulos, N.: *J. Mater. sci.*, 2010, 45, (8), 2099.

Kozlova, O., Voytovych, R., Protsenko, P. and Eustathopoulos, N.: *J. Mater. sci.*, 2008, 43, (16), 5669.

Kim, J., Kang, K. and Lowengrub, J.: *J. Comput. Phys.*, 2004, 193, 511.

Krantz, T.: *Int. J. Powder Metall.*, 1969, 5, 35.

Lenel, F. V.: *Trans AIME*, 1948, 175, 878.

Lenel, F. V. and Cannon, H. S.: In *Proc. Metallwerk Plansee*, Reutte, Austria, 1953, 106.

Leger, L. and Joanny, J. F.: *Rep. Prog. Phys.*, 2011, 431.

Lesnik, N., Pestun, T. and Eremenko, V.: *Poroshkovaya Metall.*, 1971, 94, (83), 849.

Lesage, A-C., Allain, O. and Dervieux, A.: *Int. J. Num. Meth. Fluids*, 2007, 53, 1297.

Loginova, I., Ågren, J. and Amberg, G.: *Acta Mater.*, 2003, 51, 1327.

Larsson, S. and Thomee V.: *Partial differential equations with numerical methods*, Springer New York, Inc., 2003.

Metal Powder Industries Federation (MPIF), www.mpif.org, 2014.

Moon, J. R.: *Powder Metall. Int.*, 1971, 4, 194.

Mukherjee, A. and Kandlikar, S. G.: *Int. J. Heat Mass Transfer*, 2007, 50, 127.

Naidich, Y. V., Perevertailo, V. M. and Nevodnik, G. M.: *Zavod Lab.*, 1976, 1, 39.

Naidich, Y. V., Perevertailo, V. M. and Nevodnik, G. M.: *Porosh-kovaya Metallurgiya*, 1972, 7, 51.

Oro, R., Bernardo, E., Campos, M. and Torralba, J.: In *Proc. EuroPM2011*, Barcelona, Spain, October 2011, EPMA, Vol. 1, 57-62.

Oro, R., Campos, M. and Torralba, J.: *Powder Metall.*, 2012, 55, 180.

Probstein, R. F.: *Physicochemical Hydrodynamics: An Introduction*, 2nd edn. 2003, John Wiley & Sons, Inc.

Petzow, G., Kaysser, W. A. and Huppmann, W. J.: *Powder Metall.*, 1980, 2.

Price, G. H. S., Smithells, C. J. and Williams, S. V.: *J. Inst. Met.*, 1938, 62, 239.

Pelzel, E.: *Metall.*, 1955, 2, 565.

Pejovnik, S., Kolar D., Huppmann, W. J. and Petzow, G.: In *Sintering - New Developments* , Amsterdam, Netherlands, 1979, 106.

Saad, Y.: *Iterative methods for Sparse Linear Systems*, Boston, MA: PWS Publishing Company,1996.

Schwartzkopf, P. and Kieffer, R.: *Cemented Carbides*, MacMillan, New York, NY, 1960.

Saiz, E., Tomsia, A. P., Rauch, N., Scheu, C., Ruehle, M. and Benhassine, M.: *Phys. Rev. E*, 2007, 76, 041602.

Saiz, E., Cannon, R. M. and Tomsia, A. P.: *Acta. Mater.*, 2000, 48, 4449.

Saiz, E., Benhassine, M., Coninck, J. D. and Tomsia, A.: *Scr. Mater.*, 2010, 62, 934.

Saiz, E. and Tomsia, A. P.: *Nat. Mater.*, 2004, 3, (12), 903.

Seppecher, P.: *Int. J. Eng. Sci.*, 1996, 34, 977.

Singh, P. and Joseph, D. D.: *J. Fluid Mech.*, 2005, 530, 31.

Son, G. and Hur, N.: *Num. Heat Transfer, Part B*, 2007, 48, 303.

Sussman, M., Smereka, P. and Osher, S.: *J. Comp. Phys.*, 1994, 114, 146.

Tahir, A. M., Amberg, G., Hedström, P., Bergman, O. and Frisk, K.: In *Proc. EuroPM2013*, Göteborg, Sweden, September 2013, EPMA, Vol. 2.

Tahir, A. M., Amberg, G. and Do-Quang, M.: *Acta Mater*, 2013, 61, 5375.

Thermo-Calc Software TCFE6 Steels/Fe-alloys database. http://www.thermocalc.com (Accessed 20 Feb 2013).

Tendolkar, G. S. and Sebastian, K. V.: *Powder Metall. Int.*, 1979, 11, 62.

Unverdi, S. O. and Tryggvason, G.: *J. Comp. Phys.*, 1992, 100, 25.

Villanueva, W. and Amberg, G.: *Int. J. Multiphase Flow*, 2006, 32, 1072.

Villanueva, W., Grönhagen, K., Amberg, G. and Ågren, J.: *Phys. Rev. E*, 2008, 77, 056313.

Villanueva, W., Grönhagen, K., Amberg, G. and Ågren, J.: *Comp. Mater. Sci.*, 2009, 47, 512.

Warren, R.: *Int. J. Powder Metall.*, 1977, 3, 249.

Yoon, D. N., Petzow, G., Kaysser, W. A. and Huppmann, W. J.: *Powder Metall. Int.*, 1979, 11, 50.

Yost, F. G.: *Scr. Mater.*, 1998, 38, 1225.

Yang, J., Koplik, J. and Banavar, J. R.: *Acta Mater.*, 1991, 67, 3539.

Young, T.: *Philos. Trans. Soc. London*, 1805, 95, 65.

Yue, P., Zhou, C. and Feng, J. J.: *J. Fluid Mech.*, 2010, 645, 279.

Zisman, W. A.: In *Advances in Chemistry Series 43*, Washington, D.C., New York, 1964.